

Electrical switching of Ising-superconducting nonreciprocity for quantum neuronal transistor

Junlin Xiong^{1†}, Jiao Xie^{1†}, Bin Cheng^{2*}, Yudi Dai¹, Xinyu Cui¹, Lizheng Wang¹,
Zenglin Liu¹, Ji Zhou¹, Naizhou Wang³, Xianghan Xu⁴, Xianhui Chen³, Sang-Wook
Cheong⁴, Shi-Jun Liang^{1*}, Feng Miao^{1,5*}

¹Institute of Brain-Inspired Intelligence, National Laboratory of Solid State Microstructures, School of Physics, Collaborative Innovation Center of Advanced Microstructures, Nanjing University, Nanjing 210093, China

²Institute of Interdisciplinary Physical Sciences, School of Science, Nanjing University of Science and Technology, Nanjing 210094, China

³Hefei National Laboratory for Physical Science at Microscale and Department of Physics and Key Laboratory of Strongly Coupled Quantum Matter Physics, University of Science and Technology of China, Hefei, Anhui 230026, China

⁴Center for Quantum Materials Synthesis and Department of Physics and Astronomy, Rutgers, The State University of New Jersey, Piscataway, NJ, 08854, USA

⁵Hefei National Laboratory, Hefei 230088, China

† Contribute equally to this work.

*Correspondence email: bincheng@njust.edu.cn; sjliang@nju.edu.cn;
miao@nju.edu.cn

Abstract: Nonreciprocal quantum transport effect is mainly governed by the symmetry breaking of the material systems and is gaining extensive attention in condensed matter physics. Realizing electrical switching of the polarity of the nonreciprocal transport without external magnetic field is essential to the development of nonreciprocal quantum devices. However, electrical switching of superconducting nonreciprocity remains yet to be achieved. Here, we report the observation of field-free electrical switching of nonreciprocal Ising superconductivity in Fe₃GeTe₂/NbSe₂ van der Waals (vdW) heterostructure. By taking advantage of this electrically switchable superconducting nonreciprocity, we demonstrate a proof-of-concept nonreciprocal quantum neuronal transistor, which allows for implementing the XOR logic gate and faithfully emulating biological functionality of a cortical neuron in the brain. Our work provides a promising pathway to realize field-free and electrically switchable nonreciprocity

of quantum transport and demonstrate its potential in exploring neuromorphic quantum devices with both functionality and performance beyond the traditional devices.

Introduction

Nonreciprocity is an inherent property of materials describing the inequality of the electric or optical signals traveling in opposite directions. This nonreciprocity is usually strongly correlated to the intricate interplay among various types of symmetry breaking, such as inversion symmetry, time-reversal symmetry and mirror symmetry¹⁻⁷. Manipulation of the nonreciprocity by switching the polarized states resulting from the spontaneous symmetry breaking could give unique opportunities for developing future technologies. Particular interest in this field lies in the nonreciprocal superconducting transport⁸⁻¹⁸, which could be exploited to develop next-generation electronic devices that have ultralow dissipation and new functionalities, such as electronic synapses and neurons¹⁹⁻²⁵. A key step for that purpose is achieving electrical switching of the nonreciprocal superconductivity without the assistant of external magnetic field, but the electrically switchable nonreciprocal superconductivity is still absent. It's worth noting that the polarity of such superconducting diode effect is usually strongly entwined with the breaking mechanisms of time-reversal symmetry and crystalline symmetry²⁶. To that end, searching unconventional superconductors with magnetization- or ferroelectricity-determined nonreciprocity would give a unique opportunity for electrically switching the superconducting diode behavior by reversing those polarized symmetry-broken states^{13,27}.

In this work, we demonstrate the electrically switchable nonreciprocal Ising superconductivity at zero magnetic field in a perpendicular-anisotropy Ising-superconducting (PAIS) quantum material. The PAIS material is synthesized by stacking a layered Ising superconductor, which has Ising-type spin-orbit coupling (SOC)²⁸, onto a vdW magnet of perpendicular anisotropy²⁹. With the high-quality vdW interface, strong magnetic proximity is induced in the Ising superconductor and breaks time-reversal symmetry, leading to emergence of field-free nonreciprocal

Ising-superconductivity, *i.e.*, superconducting diode effect. Moreover, the polarity of nonreciprocal superconductivity in the PAIS device can be switched by electrically reversing the magnetization at zero magnetic field through current-induced out-of-plane spin accumulation. Based on the electrical manipulation of this magnetization-determined superconducting diode effect, the proposed nonreciprocal neuronal transistor can implement XOR logic gate and faithfully emulate the biological functionality of a cortical neuron in the brain. Our work demonstrates that the electrical switching of nonreciprocal quantum transport in the condensed matter systems shows great potential in neuromorphic computing.

Results

Field-free and magnetization-determined superconducting diode

The PAIS device was fabricated by stacking vdW magnet Fe_3GeTe_2 (FGT) and Ising superconductor 2H-NbSe_2 (Fig. 1a and 1b). We carried out measurements of the longitudinal resistance under different temperatures. A typical PAIS device with five-layer NbSe_2 (see the atomic force microscope images and corresponding height profiles in Supplementary Fig. 1) exhibits a superconducting behavior with a transition temperature of $T_c \approx 2.95$ K (Fig. 1c). To characterize the magnetization of the PAIS material, we measured the Hall resistance under various magnetic field (Supplementary Fig. 2). The results show hysteresis loops of Hall resistance which shrink as temperature increases, indicating that the PAIS device possesses switchable perpendicular magnetization states, denoted as magnetization “UP” and “DOWN” states.

We then investigated the superconducting behaviors under different magnetization states. We first set the magnetization state of the device as “UP” and swept the d.c. current under different perpendicular magnetic fields B_z , and monitored the longitudinal resistance at the temperature of 1.6 K. As shown in Fig. 1d, sharp jumps of resistance occur as the current reaches a critical value ($|I_c|$). When B_z is applied in the positive direction of the z-axis (*e.g.*, $B_z = +10$ mT), $|I_c|$ strongly depends on the direction of the current flowing (positive $+I$ or negative $-I$), indicating

the nonreciprocity of the supercurrent, *i.e.*, superconducting diode effect. Such nonreciprocal supercurrent, characterized by $\Delta I_c = |I_c^+| - |I_c^-|$, is dependent on the applied magnetic field, as shown in Fig. 1e. Here, $\Delta I_c > 0$ and $\Delta I_c < 0$ corresponds to the “+” and “-” polarity, respectively. Notably, as B_z is set to zero, a significant nonreciprocal supercurrent with “+” polarity still exists, suggesting the emergence of superconducting diode effect does not require external field. This nonreciprocity with “+” polarity is retained until $B_z = -10$ mT and eventually reversed to that with “-” polarity (*i.e.*, $\Delta I_c < 0$). When the magnetic field further increases, the nonreciprocal supercurrent ΔI_c is then suppressed beyond certain magnetic field due to field-induced breakdown of superconductivity (Supplementary Fig. 5). In contrast, we observed the nonreciprocal supercurrent with same magnitude but opposite polarity, when the magnetization is switched to the “DOWN” state (Fig. 1f-g). Such nonreciprocity of superconducting transport can persist to zero external magnetic field in our PAIS device. This is in stark contrast to that reported in nonmagnetic superconducting device⁸, in which the nonreciprocal superconducting transport only emerges at non-zero external magnetic field. Such zero-field superconducting diode effect can produce a large nonreciprocal efficiency, defined by $\eta = \frac{2(|I_c^+| - |I_c^-|)}{|I_c^+| + |I_c^-|}$, up to 13% at 1.6 K, which is much larger than the value (6% at 0.9 K) previously reported in NbSe₂-based heterostructure¹⁶. Since the direction of electrical transport is perpendicular to the magnetization, the observed nonreciprocal superconductivity is similar to magneto-toroidal nonreciprocal directional dichroism (NDD) effect⁵. Note that the nonreciprocal superconducting behavior is determined by the magnetization state in our PAIS device. Electrical switching of the magnetization is thus critical for developing ultralow-power electronic devices based on the superconducting diode effect.

Field-free electrical switching of superconducting diode

We demonstrated that such electrical switching of the polarity of nonreciprocal superconductivity in the PAIS device can be realized through d.c. current pulse. We

first swept the pulsed d.c. current I_{pulse} applied to the PAIS device at 1.6 K and monitored the change in the Hall resistance, with the corresponding results presented in Fig. 2a. At zero magnetic field, sweeping I_{pulse} upwards or downwards to a critical value can change the sign of the Hall resistance. This phenomenon is consistent with the anomalous Hall effect observed in the same device (Fig. 2b), confirming that the d.c. current pulse can switch the magnetization state in the PAIS device. To be specific, a positive current pulse favours the reversal of the magnetization to “UP” state, while a negative current pulse switches the magnetization to “DOWN” state. Such field-free electrical switching of magnetization could enable the electrical manipulation of nonreciprocal superconducting transport due to the intrinsic intertwinement of magnetization and nonreciprocal superconductivity. As shown in Fig. 2c, after applying a positive current pulse ($I_{\text{pulse}} = +10$ mA), we observed the field-free nonreciprocal superconductivity with “+” polarity, consistent with the behavior of magnetization “UP” state demonstrated in Fig. 1d. By contrast, a negative current pulse ($I_{\text{pulse}} = -10$ mA) can switch the nonreciprocal superconductivity with “+” polarity to its opposite, which is consistent with the behavior of magnetization “DOWN” state shown in Fig. 1f. Such electrical switching of the nonreciprocal Ising superconductivity could provide a promising pathway for the development of novel nonreciprocal electronic devices¹⁷.

Origin of field-free electrically switchable nonreciprocal superconductivity

We infer that the nonreciprocal Ising superconductivity could result from the intricate interplay among the valley-contrasting Ising spin-orbit coupling (SOC) effect, the time-reversal symmetry breaking induced by magnetic proximity effect and the lowered rotation symmetry in the PAIS quantum materials. On the one hand, the ubiquitous strain and lattice mismatch at the vdW interface can break the \mathcal{M}_y mirror symmetry of the NbSe₂, and lead to in-plane electrical polarization (\mathbf{P}). This in-plane \mathbf{P} and perpendicular magnetization \mathbf{M} of PAIS device can form a magneto-toroidal moment³⁰, leading to magneto-toroidal NDD with nonreciprocal charge transport. When charge current is applied, such lowered lattice symmetry at the interface can give rise to valley-asymmetric Berry curvature distribution, and thus lead to valley magnetization with perpendicular anisotropy, which can generate a spin torque and facilitate the switching of magnetization in PAIS device³¹. In this case, the magneto-

toroidal NDD can be flipped by electric pulse through the flipping of \mathbf{M} with \mathbf{P} fixed.

On the other hand, with the current along the zigzag direction, the \mathcal{M}_y mirror symmetry of this system can also be broken due to the intricate interplay between valley-contrasting trigonal warping and the magnetic proximity effect (see more detailed discussion in Supplementary Materials). As shown in Fig. 3a-b, an upward magnetization enhances the spin polarization in K valley while decreases the spin polarization in K' valley. In conjunction with the asymmetric trigonal warping effects present in the two distinct valleys, a finite momentum of Cooper pairs could emerge in NbSe₂. Conversely, a downward magnetization gives rise to the non-zero Cooper pairs momentum in an opposite manner (Fig. 3c-d). Notably, such effect is a quadratic effect compared to the fermi energy which dominates the charge transport properties. However, the superconducting gap is several orders smaller than the fermi energy, leading to prominent nonreciprocal quantum transport behavior near the superconducting region where superconducting gap is the dominant energy scale. Such understanding can be further verified by our successful observation of prominent second harmonic behavior near the superconducting transition region (see Supplementary Fig. 6 and Methods for details), which decays fast when the superconductivity is fully suppressed by external magnetic field and the fermi energy becomes the dominate energy scale. To further clarify this mechanism, we employ the generalized Ginzburg-Landau (GL) theory^{3,32} in the proximity to the transition temperature T_c (see methods for details). When the magnetic proximity and trigonal warping effect is considered in the Ising superconductor NbSe₂, we demonstrate that the nonreciprocity of superconducting transport is determined by both the external magnetic field B_z and the proximity-induced magnetization M_z , which is consistent with our experimental results shown in Fig. 2. In addition, the nonreciprocal efficiency η is calculated to be proportional to $(T_c - T)^{1/2}$, which coincides with our experimental result shown in Supplementary Fig. 7 (see details in Methods). Finally, the calculation shows that the valley-contrasting Ising SOC with trigonal warping effect could also facilitate the generation of current-induced perpendicular spin polarization (see Methods for details), as shown in the inset of Fig. 3e. This current-induced z-spin could also produce a spin torque at the vdW interface and thus contribute to the switching of the magnetization in the PAIS material (Supplementary Fig. 8). It is noted that this electrically switchable nonreciprocal superconductivity is

reproducible and observed in the both PAIS devices with odd-layer and even-layer NbSe₂ (see Section IX of the Supplementary Materials). Fully understanding of such electrical switching of superconducting nonreciprocity requires microscopic models considering the details of the magnetic proximity effect and the symmetry breaking at the vdW interface^{27,33-35}.

Quantum neuronal transistor based on electrically switchable superconducting diode effect

Taking advantage of the electrically switchable nonreciprocal Ising superconductivity, we propose and demonstrate a proof-of-concept quantum neuronal transistor, which can faithfully emulate the biological functionality of a cortical neuron³⁶ in the brain, *i.e.*, performing nonlinear computing operations (Fig. 4a). The neural transistor, a tetrode device shown in Fig. 4b, is operated by feeding input and control signals (represented by X and Y) into the NbSe₂ film through the electrodes. The control current pulse signal Y is used for deterministic reversal of the perpendicular magnetization and thus determines the polarity state (“ $\Delta I_c > 0$ ” and “ $\Delta I_c < 0$ ” corresponds to state “1” and “0”, respectively) of nonreciprocal superconducting transport. The resulting state would generate a distinct electrical output corresponding to the input current signal X. The output state (“1” or “0”) is represented by the resistance (high or low). To demonstrate the function of the proposed transistor, we switched the polarity state of nonreciprocal superconductivity by applying a train of positive and negative current pulses (denoted as I_{switch}) onto this device (Fig. 4c) and measured the resulting output (Fig. 4d). For the probe current I_{probe} of +39 μA , the ON-state resistance (R_{ON}) corresponding to the polarity “+” state is smaller than 0.004 Ω , whereas the OFF-state resistance (R_{OFF}) corresponding to the polarity “-” state is about 9.8 Ω , giving rise to an on/off ratio of 10^3 . This value is two order of magnitude larger than that of MgO-based conventional MTJs³⁷⁻³⁹ and one order of magnitude larger than the state-of-the-art value (1,9000%) under similar experimental conditions⁴⁰. Notably, this ratio depends on the lowest resolution of the measurement system and can be further improved by improving the detection

precision. We also note that a superconducting transistor based on the distinct physical mechanism has been theoretically proposed in a Josephson junction with chiral magnet⁴¹. Unlike the Josephson transistor based on the junction structure in that work, our proposed superconducting neuronal transistor is realizable in all-metallic junction-free superconductors.

The quantum neuronal transistor can emulate the biological function of a cortical neuron³⁶ in the brain, which can classify linearly non-separable inputs. As the polarity of nonreciprocity is in “+” state, the transistor exhibits a threshold response behavior due to current induced transition between the superconducting and normal states, and only spikes (*i.e.* output jumps from state “0” to state “1” and back to state “0”) when receiving negative current pulses of large magnitude (Fig. 4e). In contrast, the transistor with polarity “-” state only spikes when receiving positive current pulses of large magnitude. These threshold response behaviors resemble those features in the cortical neurons capable of executing XOR nonlinear computational function. Moreover, we show that the neuronal transistor can also realize the function of XOR gate (Fig. 4f). To demonstrate the XOR function, we set the positive current pulse (+39 μA) as input logic state ‘1’ and the negative current pulse (-39 μA) as input logic state ‘0’ in the experiment. As shown in Fig. 4g, when the input state and polarity state are set to (0,1) and (1,0), logic state “1” corresponding to a high resistance can be generated. By contrast, logic state “0” corresponding to a low resistance can be output when the input state and polarity state are set to (0,0) and (1,1). These results indicate that an XOR gate can be realized in a single quantum transistor. Note that this nonlinear Boole logic function cannot be implemented with a single traditional device and is conventionally thought to require multilayered networks⁴²⁻⁴⁴. In addition, the PAIS device allows the simultaneous achievement of the giant on/off ratio (>200,000%) and ultralow resistance area product ($\approx 0.1 \Omega \cdot \mu\text{m}^2$), which cannot be realized in conventional MTJs (see detailed comparison in Supplementary Fig. 12) but urgently required for ultrahigh-density electronic applications^{45,46}.

Discussion

In summary, we demonstrate field-free electrical switching of Ising superconducting diode effect in the $\text{Fe}_3\text{GeTe}_2/\text{NbSe}_2$ van der Waals (vdW) heterostructure. By taking advantage of this electrically switchable superconducting

diode effect, we propose and demonstrate a nonreciprocal quantum neuronal transistor able to perform the XOR function, which is inaccessible with previously reported technology. Our work opens up a promising avenue for neuromorphic computing based on nonreciprocal quantum transport.

Methods

Device fabrication and fundamental characterization

We mechanically exfoliated the NbSe₂ and FGT flakes onto a highly doped Si wafer covered by a 300-nm-thick SiO₂ layer. Before the device fabrication, the crystallographic orientation of the NbSe₂ flake was characterized by measuring the co-polarized SHG intensity as a function of relative angle between laser polarization and crystal orientation. In the following fabrication process, we designed the device geometry to set the direction of current along zigzag direction of the NbSe₂ sample in the experiments. As shown in Supplementary Fig. 14, the maximum (minimum) intensity corresponds to the armchair (zigzag) direction of the crystal, confirming the current flowing along the zigzag direction. The thickness of these flakes were identified with optical contrast and a Bruker MultiMode 8 atomic force microscope. The NbSe₂ and FGT flakes of typical PAIS device are approximately 3.1 nm (5 layers) and 28.9 nm in thickness, respectively (see the atomic force microscope images and corresponding height profiles in Supplementary Fig. 1). The bottom electrodes (2 nm Ti/30 nm Au) were patterned using the standard electron beam lithography method and deposited by standard electron beam evaporation. Poly(propylene) carbonate (PPC) coated on polydimethylsiloxane (PDMS) was used to pick up the NbSe₂ and FGT flakes and fabricate the heterostructure devices in a glovebox filled with an inert atmosphere to avoid degradation.

Electrical measurements

All the electrical measurements were performed in the Oxford cryostat with magnetic fields of up to 14 T and temperatures between 1.5 and 300 K. To characterize the electric transport state, a Keithley 2636B dual-channel digital source meter or lock-in amplifier (Stanford SR830) was used to inject the d.c. or a.c. current and measure the 4-probe resistance. The a.c. measurements were performed by

injecting a.c. current with a frequency of ω (17.777 Hz) using lock-in amplifiers (Stanford SR830). In the measurement of electrical switching of magnetization, large current pulses (write current, 200 μ s) were first applied by using Keithley 2636B dual-channel digital source meter. After an interval of 5s, the Hall resistance was measured using an alternating current excitation current of 500 μ A.

Effective tight-binding Hamiltonian

For a NbSe₂/FGT heterostructure, the tight-binding Hamiltonian⁴⁷⁻⁵⁰ can be given by

$$H(\mathbf{k}) = \varepsilon(\mathbf{k}) + h_{Ising}(\mathbf{k}) + h_{proximity} \quad (1)$$

where $\varepsilon(\mathbf{k}) = -\sum_{j=1}^3\{2t_1 \cos k_j + 2t_2 \cos(k_j - k_{j+1})\} - \mu$ is the kinetic energy with $k_j = \mathbf{k} \cdot \mathbf{R}_j$, and the unit lattice vectors $\mathbf{R}_1 = \hat{\mathbf{y}}$, $\mathbf{R}_2 = -\frac{\hat{\mathbf{y}}}{2} - \frac{\sqrt{3}}{2}\hat{\mathbf{x}}$, $\mathbf{R}_3 = -\frac{\hat{\mathbf{y}}}{2} + \frac{\sqrt{3}}{2}\hat{\mathbf{x}}$, $\mathbf{R}_4 \equiv \mathbf{R}_1$. Here μ is the chemical potential, t_1 and t_2 denote the nearest-neighbor (NN) and next-nearest-neighbor (NNN) hopping integrals, respectively. $h_{Ising}(\mathbf{k}) = -\beta(\mathbf{k})\sigma_z$ is the energy caused by Ising spin-orbit coupling originated from inversion symmetry breaking of NbSe₂, where $\beta(\mathbf{k}) = \lambda_I(\sin k_1 + \sin k_2 + \sin k_3)$. $h_{proximity} = -M_z\sigma_z$ is the energy caused by the proximity effect from the perpendicular magnetization. We set $(t_1, t_2, \mu, \lambda_I) = (0.009, -0.093, 0, 0.025)$ eV to fit the electronic band structure from DFT calculations^{49,51}. The band structure and spin texture of NbSe₂ for different magnetization states are shown in Fig.3(a) and (c) in the main text. As shown in Fig. 3(a), an upward magnetization enhances the spin polarization in K valley while decreases the spin polarization in K' valley, thereby lifting the valley degeneracy. Conversely, a downward magnetization can lift the valley degeneracy in a opposite manner (Fig. 3c).

Nonreciprocal critical current originated from finite momentum

We employ the generalized Ginzburg-Landau (GL) theory^{3,32} to elucidate the magnetization-determined nonreciprocal superconductivity in our PAIS device. The effective Hamiltonian of PAIS material is given by,

$$H(\mathbf{k}) = \varepsilon(\mathbf{k}) + h_{Ising}(\mathbf{k}) + h_{proximity} \quad (2)$$

where $\varepsilon(\mathbf{k}) = \frac{\hbar^2 \mathbf{k}^2}{2m} - \mu$ is the kinetic energy with $\mathbf{k} = (k_x, k_y)$, $h_{Ising}(\mathbf{k}) = \lambda_I \sigma_3 + \gamma k_x (k_x^2 - 3k_y^2) \sigma_3$ and $h_{proximity} = H_z^{eff} \sigma_3$ are the energy of the Ising spin-orbit interaction and the magnetic proximity effect, respectively. Here, $H_z^{eff} \equiv B_z + \kappa M_z$ is defined as an effective field contributed from the external magnetic field B_z and the proximity perpendicular magnetization M_z . Here, κ is a constant to ensure dimensional consistency. The effective Hamiltonian $H(\mathbf{k})$ has the mirror symmetry \mathcal{M}_x since $\mathcal{M}_x H(k) \mathcal{M}_x^{-1} = H(k)$, but breaks the mirror symmetry \mathcal{M}_y since $\mathcal{M}_y H(k) \mathcal{M}_y^{-1} \neq H(k)$.

To derive the microscopic GL free energy, the mean-field Hamiltonian is given by

$$H_{MF}(\Delta, \mathbf{q}) = \frac{1}{2} \sum_{\mathbf{k}} \Psi^\dagger(\mathbf{k}, \mathbf{q}) \mathcal{H}(\mathbf{k}, \mathbf{q}) \Psi(\mathbf{k}, \mathbf{q}) + const, \quad (3)$$

where $\mathcal{H}(\mathbf{k}, \mathbf{q}) = \begin{pmatrix} H(\mathbf{k} + \mathbf{q}) & \Delta i \sigma_2 \\ -\Delta i \sigma_2 & -H^\tau(-\mathbf{k}) \end{pmatrix}$ represents the BdG Hamiltonian and $\Psi(\mathbf{k}, \mathbf{q}) = (c_{\mathbf{k}+\mathbf{q}\uparrow}, c_{\mathbf{k}+\mathbf{q}\downarrow}, c_{-\mathbf{k}\uparrow}^\dagger, c_{-\mathbf{k}\downarrow}^\dagger)^\tau$ is the Nambu spinor. Here, τ denotes transpose.

The free energy density can be expressed as a functional of the superconducting order parameter Δ ,

$$f_s(\Delta, \mathbf{q}) \equiv -T \ln \text{Tr} \exp \left(-\frac{H_{MF}(\Delta, \mathbf{q})}{T} \right), \quad (4)$$

where T is the temperature and the Boltzmann constant k_B is neglected for simplicity¹⁰. We expanded the free energy density up to the third order of \mathbf{q} and the first order of λ_I and γ , that is,

$$f_s(\Delta, \mathbf{q}) = [\alpha_0 + \alpha_2 \mathbf{q}^2 + \alpha_3 q_x (q_x^2 - 3q_y^2) B_z^{eff}] |\Delta|^2 + \frac{\beta}{2} |\Delta|^4, \quad (5)$$

where $\alpha_0 = A_0(T - T_c)$, $\alpha_2 = \frac{\hbar^2}{4m}$, $\alpha_3 = A_3 \frac{\lambda_I \gamma}{T_c^2}$ and $\beta > 0$ with $A_0, A_3 > 0$ are numerical constants.

For simplicity, we express the above free energy density in a more compact form, $f_s(\Delta, \mathbf{q}) = \alpha(\mathbf{q})|\Delta|^2 + \frac{\beta}{2}|\Delta|^4$, with $\alpha(\mathbf{q}) = \alpha_0 + \alpha_2 \mathbf{q}^2 + \alpha_3 q_x (q_x^2 - 3q_y^2) B_z^{eff}$. Denoting θ as the angle between \mathbf{q} and q_x axis, *i.e.*, $q_x = q \cos \theta$ and $q_y = q \sin \theta$, we then can obtain

$$\alpha(\mathbf{q}) = \alpha_0 + \alpha_2 \mathbf{q}^2 + \alpha_3 \mathbf{q}^3 \cos 3\theta B_z^{eff}. \quad (6)$$

Additionally, the order parameter can be optimized by $\frac{\partial f}{\partial |\Delta|^2} = \alpha(\mathbf{q}) + \beta |\Delta|^2 = 0$, *i.e.*, $|\Delta|^2 = -\frac{\alpha(\mathbf{q})}{\beta}$ with $\alpha(\mathbf{q}) < 0$, leading to

$$f_s(\mathbf{q}) = -\frac{\alpha(\mathbf{q})^2}{2\beta}. \quad (7)$$

Notice that the momentum dependent current is given by $I(\mathbf{q}) = 2 \frac{\partial f_s(\mathbf{q})}{\partial \mathbf{q}}$, which is equivalent to $\frac{\beta}{2} I(\mathbf{q}) = |\alpha(\mathbf{q})| \frac{\partial \alpha(\mathbf{q})}{\partial \mathbf{q}}$ according to Eq. (7). By minimizing $\alpha(\mathbf{q})$ over \mathbf{q} , one can find the Cooper pair momentum \mathbf{q}_0 in the equilibrium state. With current flowing along the zigzag direction, this current $I = I \hat{\mathbf{x}}$ would change this Cooper pair momentum to $q_x = (\mathbf{q} - \mathbf{q}_0) \cdot \hat{\mathbf{x}}$, then $\alpha(q_x) = \alpha_0 + \alpha_2 q_x^2 + \alpha_3 q_x^3 \hat{\mathbf{x}} \cdot (\mathbf{B}_z^{eff} \times \hat{\mathbf{y}})$. By minimizing $\alpha(q_x)$ over q_x , we find the Cooper pair momentum in the equilibrium state,

$$q_x^0 = \frac{2\alpha_0}{3\alpha_3} \hat{\mathbf{x}} \cdot (\mathbf{B}_z^{eff} \times \hat{\mathbf{y}}),$$

which is a direct result of the mirror symmetry \mathcal{M}_y breaking. In this case, we can expand $\alpha(q_x)$ around its minimum q_x^0 ,

$$\alpha(q) = \alpha_0 + \alpha_2 \delta q^2 + \tilde{\alpha}_3 \delta q^3, \quad (8)$$

where $\tilde{\alpha}_3 \equiv \alpha_3 B_z^{eff}$ and δq is define as $\delta q \equiv q_x - q_x^0$. Under this condition, we find the supercurrent is

$$\frac{\beta}{2}I(q) = 2\alpha_0\alpha_2\delta q + 3\alpha_0\tilde{\alpha}_3\delta q^2 + 2\alpha_2^2\delta q^3 + 5\alpha_1\tilde{\alpha}_3\delta q^4 + 3\tilde{\alpha}_3^2\delta q^5. \quad (9)$$

The critical momentum $\delta q_c = \sqrt{|\frac{\alpha_0}{3\alpha_2}|}$ is then given by $\partial_{\delta q}I(q)|_{\delta q=\delta q_c} = 0$. In this way, we can obtain the critical currents I_c^\pm corresponding to $\delta q = \mp\delta q_c$ respectively,

$$\frac{\beta}{2}I_c^\pm = \frac{4|\alpha_0|^{\frac{3}{2}}}{9\alpha_2} \left((3\alpha_2^3)^{\frac{1}{2}} \pm \tilde{\alpha}_3|\alpha_0|^{\frac{1}{2}} \right) + o\left(|\alpha_0|^{\frac{5}{2}}\right). \quad (10)$$

As such, the nonreciprocal efficiency is given by

$$\eta \equiv \frac{2(I_c^+ - I_c^-)}{I_c^+ + I_c^-} = \alpha_3 \left(\frac{4|\alpha_0|}{3\alpha_2^3} \right)^{\frac{1}{2}} (B_z + \kappa M_z), \quad (11)$$

showing the temperature dependence ($\eta \propto (T - T_c)^{\frac{1}{2}}$) and magnetism dependence ($\eta \propto B_z + \kappa M_z$) of nonreciprocal efficiency.

Second harmonic signals

We adopted the well-established time-dependent GL equation, as widely used in previous reports^{3,52}, to calculate the second harmonic signal in our device. By introducing a uniform electric field \mathbf{E} and setting the vector potential $\mathbf{A} = -\mathbf{E}t$, the GL free energy quadratic in the order parameter reads

$$F = \int d\mathbf{r} \Delta^*(\mathbf{r}, t)\alpha(\mathbf{r}, t)\Delta(\mathbf{r}, t) = \sum_{\mathbf{q}} \alpha(\mathbf{q}, t)|\Delta(\mathbf{q}, t)|^2, \quad (12)$$

where $\alpha(\mathbf{q}, t)$ is the time-dependent GL coefficient which can be expressed as

$$\alpha(\mathbf{q}, t) = \alpha_0 + \alpha_2 \left(\mathbf{q} - \frac{2e}{\hbar}\mathbf{E}t \right)^2 + \alpha_3 H \left(q_x - \frac{2e}{\hbar}E_x t \right) \left(\left(q_x - \frac{2e}{\hbar}E_x t \right)^2 - 3 \left(q_y - \frac{2e}{\hbar}E_y t \right)^2 \right). \quad (13)$$

Here, H is the generalized magnetic field (*i.e.*, $H = B + \kappa M$) and $\alpha_3 = A_3 \frac{\lambda_{IY}}{T_c^2}$ originated from Ising SOC. The expectation value of the excess current density can be calculated by the time-dependent GL equation with a stochastic force, namely

$$\hbar D \frac{\partial \Delta(\mathbf{r}, t)}{\partial t} = -\alpha(\mathbf{r}, t)\Delta(\mathbf{r}, t) + f(\mathbf{r}, t), \quad (14)$$

where D is the damping term for $\Delta(\mathbf{r}, t)$ resulting from the superconducting fluctuation, and $f(\mathbf{r}, t)$ is a stochastic force which generates $\langle |\Delta(\mathbf{q})|^2 \rangle = \frac{k_B T}{\alpha(\mathbf{q})}$. The solution of the time-dependent GL equation is given by

$$\Delta(\mathbf{q}, t) = \frac{1}{\hbar D} \int_{-\infty}^t dt' f(\mathbf{q}, t') \exp\left(-\frac{1}{\hbar D} \int_{t'}^t d\tau \alpha(\mathbf{q}, \tau)\right), \quad (15)$$

which also satisfies the boundary condition $\alpha(\mathbf{q}, \infty) = 0$. Then, the expectation value of the order parameter is

$$\langle |\Delta(\mathbf{q}, t)|^2 \rangle = \frac{2k_B T}{\hbar D} \int_{-\infty}^t dt' f(\mathbf{q}, t') \exp\left(-\frac{1}{\hbar D} \int_{t'}^t d\tau \alpha(\mathbf{q}, \tau)\right). \quad (16)$$

In analytical mechanics \mathbf{A} can enter through the free energy (More generally, the Lagrangian). Considering infinitesimal variations $\delta \mathbf{A}$, we get $\delta F = -\int d\mathbf{r} \mathbf{J} \cdot \delta \mathbf{A}$, an expression used to obtain the current density \mathbf{J} . Thus, the current density operator is expressed as

$$\mathbf{J}(t) = -\frac{\delta F}{\Omega \delta \mathbf{A}} = \frac{1}{\Omega} \sum_{\mathbf{q}} \left(-\frac{\partial \alpha(\mathbf{q}, t)}{\partial \mathbf{A}} \right) |\Delta(\mathbf{q}, t)|^2 = \frac{1}{\Omega} \sum_{\mathbf{q}} \mathbf{J}(\mathbf{q}, t) |\Delta(\mathbf{q}, t)|^2 \quad (17)$$

with Ω is the volume of the system. The expectation value of the current density is

$$\mathbf{J}(t) = \frac{2k_B T_c}{\Omega \hbar D} \sum_{\mathbf{q}} \int_{-\infty}^t dt' \mathbf{J}(\mathbf{q}, t') \exp\left(-\frac{1}{\hbar D} \int_{t'}^t d\tau \alpha(\mathbf{q}, \tau)\right). \quad (18)$$

By applying Eq. (13), (18), we can obtain the conductivity as

$$\mathbf{J} = \sigma_1 \mathbf{E} + \sigma_2 F(\mathbf{E}), \quad (19)$$

where $\sigma_1 = \frac{e^2}{16\hbar} \left(\frac{T_c}{T-T_c} \right)$ and $\sigma_2 = -\frac{\pi e^3 m \alpha_3 (H+o(H^3))}{64 \hbar^3 k_B T_c} \left(\frac{T_c}{T-T_c} \right)^2$. In this context, $F(\mathbf{E}) = (E_x^2 - E_y^2, -2E_x E_y)$ denotes the nonlinear term of the in-plane electric field. As expected, σ_2 encapsulates the second harmonic signal, which is prominent near the

superconducting transition where the small superconducting gap dominates the electrical transport.

We then performed the second harmonic measurement^{3,53} with sweeping the perpendicular magnetic field at 4.5 K, which corresponds to the superconducting transition regime, for both magnetization “UP” and “DOWN” states. To distinguish the linear and nonlinear component, both the first (R^ω) and second harmonic signals ($R^{2\omega}$) of the longitudinal magnetoresistance (Supplementary Fig. 6) are measured using a lock-in amplifier and applying the a.c. excitation current with an amplitude of 8 μA . The superconducting state fades off by increasing the magnetic field, manifested as the magnetoresistance in Supplementary Fig. 6a. We note that the magnetoresistance dip can be shifted to the left or right when the magnetization is reversed from “UP” to “DOWN” state, again indicating the presence of the proximity-induced exchange field κM from the magnetization of FGT. We then extracted the value of $\kappa M = \pm 10$ mT, which is consistent with the critical field B_C at which the ΔI_c vanishes for magnetization “UP” and “DOWN” state (Fig. 1e and Fig. 1g). In addition, the result that the $R^{2\omega}$ is antisymmetric with respect to the perpendicular magnetic field and magnetization (Supplementary Fig. 6b), *i.e.*, $R^{2\omega}(-B_z, M_{\text{DOWN}}) = -R^{2\omega}(B_z, M_{\text{UP}})$, which is consistent with the magneto-toroidal nonreciprocal effect. Notably, the second harmonic signal decays fast as the external magnetic field further increases and the fermi energy becomes the dominate energy scale. This phenomenon confirms the important role of trigonal warping effect on the nonreciprocal superconducting transport in our PAIS device.

Temperature dependence of nonreciprocal superconducting transport

We swept the direct current and monitored the change in resistance under various temperatures ranging from 1.6 to 3.5 K when fixing the magnetization “DOWN” state in a PAIS device with 7-layer NbSe₂ (Supplementary Fig. 7a). For each temperature, we observed significant nonreciprocal supercurrent with polarity “+” state (represented as $\Delta I_c < 0$). To further clarify the temperature dependence of this

nonreciprocal effect, the temperature dependence of nonreciprocal efficiency $|\eta| = 2 \left| \frac{I_c^+ + I_c^-}{I_c^+ - I_c^-} \right|$ are clearly plotted in Supplementary Fig. 7b. With increasing the temperature, this nonreciprocal efficiency $|\eta|$ decreases and its temperature dependence is well fitted by a $\sqrt{1 - \frac{T}{T_c}}$ function (the critical temperature $T_c = 4.8$ K see in Supplementary Fig. 7c), consistent with the theoretic analysis (see Methods: Nonreciprocal critical current originated from finite momentum).

Current-induced spin polarization

The coexistence of Ising SOC and trigonal warping at the Fermi surface can also facilitate the generation of current-induced perpendicular spin polarization. Specifically speaking, the electric field generated from charge current would change the trigonally warped Fermi surfaces of spin-up and spin-down branches in both K and K' valleys and thus lifts the valley degeneracy. This valley population imbalance would generate a z-spin polarization (the inset of Fig. 3e), which could produce a spin torque at the vdW interface and thus switch the magnetization in the PAIS material (Supplementary Fig. 8). To further elucidate the current-induced z-spin polarization, we calculated the current contribution to spin polarization using the Boltzmann equation^{34,54} as follows.

The effective Hamiltonian of a monolayer NbSe2 can be written as

$$H_{eff}(\mathbf{k}) = \frac{\hbar^2 \mathbf{k}^2}{2m} + \gamma k_x (k_x^2 - 3k_y^2) \tau_z, \quad (20)$$

where $\tau_z = \pm 1$ represent the valley degrees of freedom. Straightforward diagonalization of this Hamiltonian gives the eigenvalues

$$\varepsilon_{\pm}(\mathbf{k}) = \frac{\hbar^2 \mathbf{k}^2}{2m} \pm \gamma k_x (k_x^2 - 3k_y^2), \quad (21)$$

and eigenvectors

$$\begin{aligned} \psi_{\mathbf{k},+} &= \begin{pmatrix} 1 \\ 0 \end{pmatrix} e^{i\mathbf{k}\cdot\mathbf{r}}, \\ \psi_{\mathbf{k},-} &= \begin{pmatrix} 0 \\ 1 \end{pmatrix} e^{i\mathbf{k}\cdot\mathbf{r}}. \end{aligned}$$

For simplicity, we consider a line in the Brillouin zone along the k_x direction (*i.e.*, k_y is a good quantum number). Solving the equation $\varepsilon_{\pm}(k_{F,\pm}) = \varepsilon_F$ to first order in γ

gives

$$k_{F,\pm} \approx k_F \left(1 \mp \frac{m\gamma k_F}{\hbar^2} \right) \equiv k_F (1 \mp \xi), \quad (22)$$

with $\xi = \frac{m\gamma k_F}{\hbar^2}$. Introducing an external electric field \mathcal{E} could displace the Fermi surfaces by an amount $\Delta \mathbf{k}_\pm = -\frac{e\mathcal{E}\tau_\pm}{\hbar}$, where τ_\pm are the different energy-dependent scattering rates. Generally, one can assume that $\tau_\pm = \tau(1 \pm \xi)$ with τ the relaxation time of the free-electron gas⁵⁵.

Then we calculate analytically the current contribution from each subband using the Boltzmann equation^{34,54}, one can get

$$\mathbf{J}_\pm = -e \int \mathbf{v}_{k,\pm} \frac{\partial f_{k,\pm}}{\partial \varepsilon} e v_{k,\pm} \tau_\pm \cdot \boldsymbol{\varepsilon} d\mathbf{k} = \frac{e^2 \tau_\pm}{4\pi^2 \hbar} \iint \frac{\mathbf{v}_{k,\pm}}{v_{k,\pm}} \mathbf{v}_{k,\pm} \cdot \boldsymbol{\varepsilon} d\mathcal{S}_{F_\pm}, \quad (23)$$

where $f_{k,\pm}$ and \mathcal{S}_{F_\pm} are the electron distribution function and Fermi surfaces for the \pm bands, respectively. By choosing $\boldsymbol{\varepsilon} = \mathcal{E} \hat{\mathbf{x}}$ and assuming $v_{F,\pm} = v_F$, one can further get

$$J_{x,\pm} = \frac{e^2 \tau_\pm \mathcal{E}}{4\pi^2 \hbar} \int_0^{2\pi} v_F \cos^2 \phi k_{F,\pm} d\phi = \frac{e^2 \mathcal{E}}{4\pi \hbar} v_F k_{F,\pm} \tau_\pm, \quad (24)$$

where we apply the relation $\mathbf{k} = k(\cos \phi, \sin \phi, 0)$. Thus, the total current density is given by

$$J = J_{x,+} + J_{x,-} = \frac{e^2 \mathcal{E}}{2\pi \hbar} v_F k_F \tau (1 + \xi^2). \quad (25)$$

The spin expectation value reads

$$\langle \mathbf{S} \rangle_{k,\pm} = \langle \psi_{k,\pm} | \mathbf{S} | \psi_{k,\pm} \rangle = \begin{pmatrix} 0 \\ 0 \\ \pm 1 \end{pmatrix}. \quad (26)$$

Therefore, the spin density can be calculated in an analogous way as

$$\langle \delta \mathbf{S} \rangle_\pm = \int \langle \delta \mathbf{S} \rangle_\pm \frac{\partial f}{\partial \varepsilon} e v_{k,\pm} \tau_\pm \cdot \boldsymbol{\varepsilon} d\mathbf{k} = \mp \frac{e\mathcal{E}}{2\pi \hbar} k_{F,\pm} \tau_\pm \hat{\mathbf{z}}, \quad (27)$$

which yields the total spin density

$$\langle \delta \mathbf{S} \rangle = \langle \delta \mathbf{S} \rangle_+ + \langle \delta \mathbf{S} \rangle_- = \frac{2e\mathcal{E}}{\pi \hbar} k_F \tau \xi \hat{\mathbf{z}}. \quad (28)$$

Consequently, from the two equations (26) (29), we can get

$$\langle \delta \mathbf{S} \rangle \approx \frac{4m^2 \gamma}{e \hbar^3} J \hat{\mathbf{z}}. \quad (29)$$

Here, we set $\gamma = 6.09 \times 10^{-21} \text{J} \cdot \text{m}^3$ based the previous literature²⁸ and obtain the

relation of current induced spin density shown in Fig. 3e.

Data availability

The data that support the findings of this study have been presented in the paper and the Supplementary Information. All source data can be acquired from the corresponding authors upon request. Source data are provided with this paper.

References

- 1 Rikken, G. L. J. A., Fölling, J. & Wyder, P. Electrical Magnetochiral Anisotropy. *Phys. Rev. Lett.* **87**, 236602 (2001).
- 2 Ideue, T. *et al.* Bulk rectification effect in a polar semiconductor. *Nat. Phys.* **13**, 578-583 (2017).
- 3 Wakatsuki, R. *et al.* Nonreciprocal charge transport in noncentrosymmetric superconductors. *Sci. Adv.* **3**, e1602390 (2017).
- 4 Tokura, Y. & Nagaosa, N. Nonreciprocal responses from non-centrosymmetric quantum materials. *Nat. Commun.* **9**, 3740 (2018).
- 5 Cheong, S.-W. SOS: symmetry-operational similarity. *npj Quantum Mater.* **4**, 53 (2019).
- 6 Yasuda, K. *et al.* Large non-reciprocal charge transport mediated by quantum anomalous Hall edge states. *Nat. Nanotechnol.* **15**, 831-835 (2020).
- 7 Guo, C. *et al.* Switchable chiral transport in charge-ordered kagome metal CsV₃Sb₅. *Nature* **611**, 461-466 (2022).
- 8 Ando, F. *et al.* Observation of superconducting diode effect. *Nature* **584**, 373-376 (2020).
- 9 Bauriedl, L. *et al.* Supercurrent diode effect and magnetochiral anisotropy in few-layer NbSe₂. *Nat. Commun.* **13**, 4266 (2022).
- 10 Daido, A., Ikeda, Y. & Yanase, Y. Intrinsic Superconducting Diode Effect. *Phys. Rev. Lett.* **128**, 037001 (2022).
- 11 Davydova, M., Prembabu, S. & Fu, L. Universal Josephson diode effect. *Sci. Adv.* **8**, eabo0309 (2022).
- 12 Jeon, K.-R. *et al.* Zero-field polarity-reversible Josephson supercurrent diodes enabled by a proximity-magnetized Pt barrier. *Nat. Mater.* **21**, 1008-1013 (2022).
- 13 Lin, J.-X. *et al.* Zero-field superconducting diode effect in small-twist-angle trilayer graphene. *Nat. Phys.* **18**, 1221-1227 (2022).
- 14 Narita, H. *et al.* Field-free superconducting diode effect in noncentrosymmetric superconductor/ferromagnet multilayers. *Nat. Nanotechnol.* **17**, 823-828 (2022).
- 15 Pal, B. *et al.* Josephson diode effect from Cooper pair momentum in a topological semimetal. *Nat. Phys.* **18**, 1228-1233 (2022).
- 16 Wu, H. *et al.* The field-free Josephson diode in a van der Waals heterostructure. *Nature* **604**, 653-656 (2022).
- 17 Nadeem, M., Fuhrer, M. S. & Wang, X. The superconducting diode effect. *Nat. Rev. Phys.* **5**, 558-577 (2023).
- 18 Trahms, M. *et al.* Diode effect in Josephson junctions with a single magnetic atom.

- Nature* **615**, 628-633 (2023).
- 19 Liu, Y. *et al.* Cryogenic in-memory computing using tunable chiral edge states. *arXiv e-prints*, arXiv:2209.09443 (2022).
- 20 Chen, J. *et al.* Topological phase change transistors based on tellurium Weyl semiconductor. *Sci. Adv.* **8**, eabn3837 (2022).
- 21 Chen, J. *et al.* Room-temperature valley transistors for low-power neuromorphic computing. *Nat. Commun.* **13**, 7758 (2022).
- 22 Liang, S.-J., Li, Y., Cheng, B. & Miao, F. Emerging Low-Dimensional Heterostructure Devices for Neuromorphic Computing. *Small Struct.* **3**, 2200064 (2022).
- 23 Chen, M. *et al.* Moiré heterostructures: highly tunable platforms for quantum simulation and future computing. *J. Semicond.* **44**, 010301 (2023).
- 24 Pan, X. *et al.* 2D materials for intelligent devices. *Sci. China Phys. Mech. Astron.* **66**, 117504 (2023).
- 25 Wang, P. *et al.* Moiré Synaptic Transistor for Homogeneous-Architecture Reservoir Computing. *Chin. Phys. Lett.* **40**, 117201 (2023).
- 26 Zhang, Y. *et al.* General Theory of Josephson Diodes. *Phys. Rev. X* **12**, 041013 (2022).
- 27 Wang, L. *et al.* Cascadable in-memory computing based on symmetric writing and readout. *Sci. Adv.* **8**, eabq6833 (2022).
- 28 Xi, X. *et al.* Ising pairing in superconducting NbSe₂ atomic layers. *Nat. Phys.* **12**, 139-143 (2016).
- 29 Deng, Y. *et al.* Gate-tunable room-temperature ferromagnetism in two-dimensional Fe₃GeTe₂. *Nature* **563**, 94-99 (2018).
- 30 Cheong, S.-W. & Xu, X. Magnetic chirality. *npj Quantum Mater.* **7**, 40 (2022).
- 31 Lee, J. *et al.* Valley magnetoelectricity in single-layer MoS₂. *Nat. Mater.* **16**, 887-891 (2017).
- 32 Yuan, N. F. Q. & Fu, L. Supercurrent diode effect and finite-momentum superconductors. *Proc. Natl Acad. Sci.* **119**, e2119548119 (2022).
- 33 Hellman, F. *et al.* Interface-induced phenomena in magnetism. *Rev. Mod. Phys.* **89**, 025006 (2017).
- 34 Manchon, A. *et al.* Current-induced spin-orbit torques in ferromagnetic and antiferromagnetic systems. *Rev. Mod. Phys.* **91**, 035004 (2019).
- 35 Liu, Y. & Shao, Q. Two-Dimensional Materials for Energy-Efficient Spin-Orbit Torque Devices. *ACS Nano* **14**, 9389-9407 (2020).
- 36 Gidon, A. *et al.* Dendritic action potentials and computation in human layer 2/3 cortical neurons. *Science* **367**, 83-87 (2020).
- 37 Parkin, S. S. P. *et al.* Giant tunnelling magnetoresistance at room temperature with MgO (100) tunnel barriers. *Nat. Mater.* **3**, 862-867 (2004).
- 38 Yuasa, S. *et al.* Giant room-temperature magnetoresistance in single-crystal Fe/MgO/Fe magnetic tunnel junctions. *Nat. Mater.* **3**, 868-871 (2004).
- 39 Ikeda, S. *et al.* Tunnel magnetoresistance of 604% at 300K by suppression of Ta diffusion in CoFeB / MgO / CoFeB pseudo-spin-valves annealed at high temperature. *Appl. Phys. Lett.* **93**, 082508 (2008).
- 40 Song, T. *et al.* Giant tunneling magnetoresistance in spin-filter van der Waals heterostructures. *Science* **360**, 1214-1218 (2018).

- 41 Hess, R., Legg, H. F., Loss, D. & Klinovaja, J. Josephson transistor from the superconducting diode effect in domain wall and skyrmion magnetic racetracks. *Phys. Rev. B* **108**, 174516 (2023).
- 42 Xia, Q. & Yang, J. J. Memristive crossbar arrays for brain-inspired computing. *Nat. Mater.* **18**, 309-323 (2019).
- 43 Kumar, S., Williams, R. S. & Wang, Z. Third-order nanocircuit elements for neuromorphic engineering. *Nature* **585**, 518-523 (2020).
- 44 Sebastian, A., Le Gallo, M., Khaddam-Aljameh, R. & Eleftheriou, E. Memory devices and applications for in-memory computing. *Nat. Nanotechnol.* **15**, 529-544 (2020).
- 45 Dieny, B. *et al.* Opportunities and challenges for spintronics in the microelectronics industry. *Nat. Electron.* **3**, 446-459 (2020).
- 46 Alam, S., Hossain, M. S., Srinivasa, S. R. & Aziz, A. Cryogenic memory technologies. *Nat. Electron.* **6**, 185-198 (2023).
- 47 Doran, N. J., Titterton, D. J., Ricco, B. & Wexler, G. A tight binding fit to the bandstructure of 2H-NbSe₂ and NbS₂. *J. Phys. C: Solid State Phys.* **11**, 685 (1978).
- 48 Kim, S. & Son, Y.-W. Quasiparticle energy bands and Fermi surfaces of monolayer NbSe₂. *Phys. Rev. B* **96**, 155439 (2017).
- 49 He, W.-Y. *et al.* Magnetic field driven nodal topological superconductivity in monolayer transition metal dichalcogenides. *Commun. Phys.* **1**, 40 (2018).
- 50 Möckli, D. & Khodas, M. Robust parity-mixed superconductivity in disordered monolayer transition metal dichalcogenides. *Phys. Rev. B* **98**, 144518 (2018).
- 51 Hörhold, S., Graf, J., Marganska, M. & Grifoni, M. Two-bands Ising superconductivity from Coulomb interactions in monolayer. *2D Mater.* **10**, 025008 (2023).
- 52 Schmid, A. Diamagnetic Susceptibility at the Transition to the Superconducting State. *Phys. Rev.* **180**, 527-529 (1969).
- 53 Rikken, G. L. J. A. & Avarvari, N. Dielectric magnetochiral anisotropy. *Nat. Commun.* **13**, 3564 (2022).
- 54 Gambardella, P. & Miron, I. M. Current-induced spin-orbit torques. *Philosophical Transactions of the Royal Society A: Mathematical, Physical and Engineering Sciences* **369**, 3175-3197 (2011).
- 55 Robert, H. S. Spin-orbit induced coupling of charge current and spin polarization. *J. Phys.: Condens. Matter* **16**, R179 (2004).

Acknowledgements

This work was supported in part by the National Key R&D Program of China under Grant 2023YFF1203600 (S.-J.L.), the National Natural Science Foundation of China (12322407 (B.C.), 62122036 (S.-J.L.), 62034004 (F.M.), 61921005 (F.M.), 12074176 (B.C.)), the National Key R&D Program of China under Grant 2023YFF0718400 (B.C.), the Leading-edge Technology Program of Jiangsu Natural Science Foundation (BK20232004 (F.M.)), the Strategic Priority Research Program of the Chinese

Academy of Sciences (XDB44000000 (F.M.)), Innovation Program for Quantum Science and Technology (F.M.). F.M. and S.-J.L. would like to acknowledge support from the AIQ Foundation. J.Z. would like to acknowledge support from the National Natural Science Foundation of China (623B1025). The microfabrication center of the National Laboratory of Solid State Microstructures (NLSSM) is acknowledged for their technique support. Crystal growth at Rutgers was supported by the center for Quantum Materials Synthesis (cQMS), funded by the Gordon and Betty Moore Foundation's EPiQS initiative through grant GBMF6402, and by Rutgers University.

Author contributions

F.M., B.C. and S.-J.L. conceived the idea and supervised the whole project. J.-L.X. fabricated few-layer devices and performed transport measurements. J.X. carried out theoretical analysis and calculations. Y.D., X.-Y.C., L.W., Z.L. and J.Z. assist the measurements. J.-L.X., J.X., B.C. and S.-J.L. analyzed the data. N.W. and X.-H.C. grew NbSe₂ bulk crystals. X.X. and S.-W.C. grew Fe₃GeTe₂ bulk crystals. J.-L.X., J.X., B.C., S.-J.L. and F.M. wrote the manuscript with input from all authors.

Competing interests

The authors declare no competing interests.

Figures

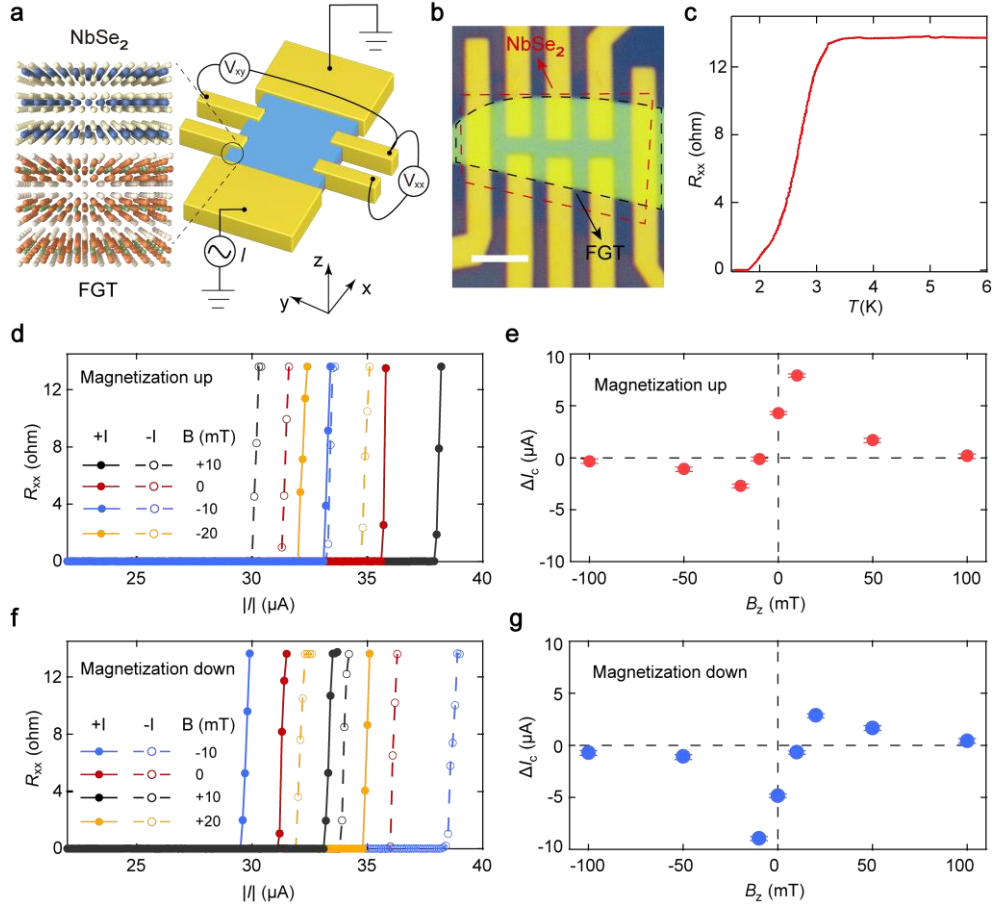


Fig. 1. Measurement configuration and magnetization-determined nonreciprocal Ising superconductivity. **a**, Schematic of the PAIS device consisting of NbSe₂ and FGT flakes for electrical transport measurements. **b**, Optical image of a typical device. The scale bar is 3 μm. **c**, Temperature dependence of the device resistance with an applied electrical current of 0.5 μA. **d**, Current dependences of the resistance under various magnetic fields for both positive and negative currents at 1.6 K when the magnetization is set as “UP” state. **e**, The nonreciprocal component of the critical current ΔI_c as a function of the magnetic field for the magnetization “UP” state. **f**, Current dependences of the resistance under various magnetic fields for both positive and negative currents at 1.6 K when the magnetization is set as “DOWN” state. **g**, The

nonreciprocal component of the critical current ΔI_c as a function of the magnetic field for the magnetization “DOWN” state.

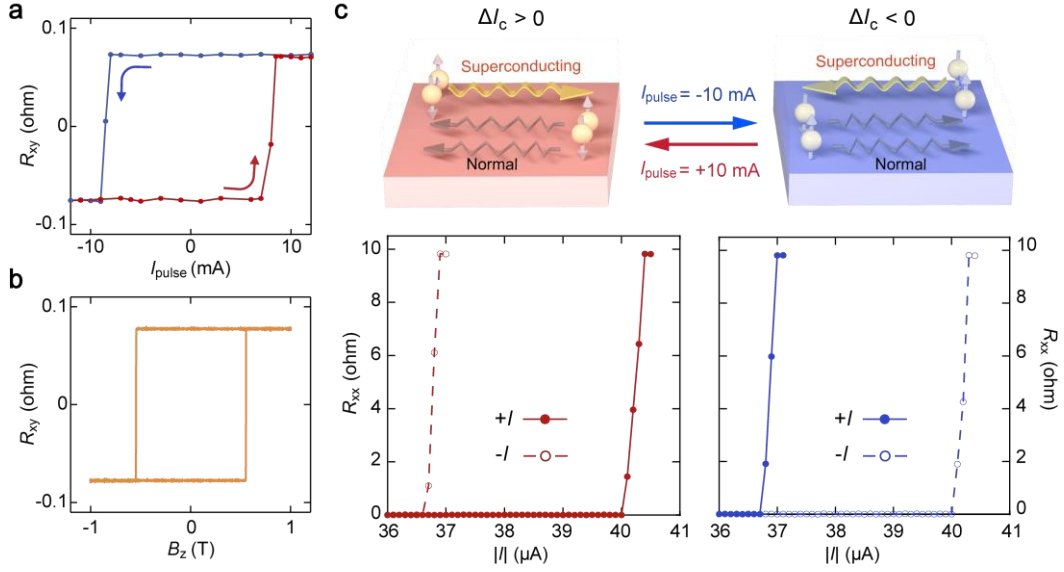


Fig. 2. Electrically switchable nonreciprocal Ising superconductivity. **a**, Current-induced magnetization switching at zero field at 1.6 K. The sign of Hall resistance is reversed by sweeping the pulsed current. **b**, Hall resistance as a function of the perpendicular magnetic field at 1.6 K. The Hall resistance was measured using an a.c. excitation current of $500 \mu\text{A}$. **c**, Schematics (upper panels) and experimental data (lower panels) of electrically switchable nonreciprocal superconducting transport. After applying a positive current pulse ($I_{\text{pulse}} = +10 \text{ mA}$), the polarity of nonreciprocal superconductivity is switched to $\Delta I_c > 0$, *i.e.*, nonreciprocal supercurrent flowing rightward (left panels). While the negative current pulse ($I_{\text{pulse}} = -10 \text{ mA}$) favours the reversal to the polarity “-” state, *i.e.*, $\Delta I_c < 0$ (right panels).

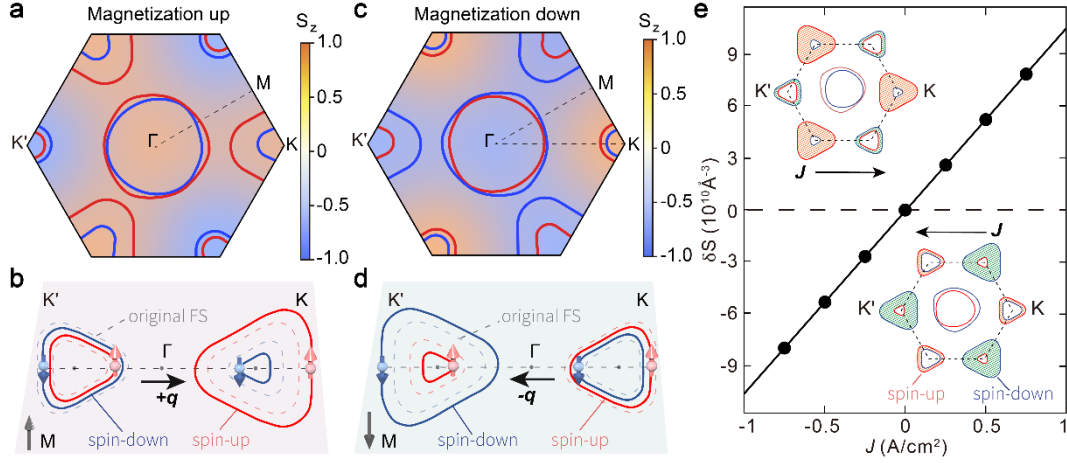


Fig. 3. The mechanism for electrically switchable superconducting diode. a, Fermi surface and spin texture of NbSe₂ based on the tight-binding Hamiltonian in the first Brillouin zone for magnetization “UP” state. The color scale indicates the out-of-plane spin component. The red and blue lines represent the energy bands with the spin “UP” and “DOWN” states, respectively. **b,** Schematic of magnetic proximity induced finite momentum of Cooper pairs for magnetization “UP” state. The dotted and solid lines represent the energy bands without and with the magnetic proximity effect, respectively. **c,** Fermi surface and spin texture of NbSe₂ for magnetization “DOWN” state. **d,** Schematic of magnetic proximity induced a finite momentum of Cooper pairs for magnetization “DOWN” state. **e,** Calculation of current-induced spin density. Insets are the schematic illustrations of spin distributions changed by the current-induced electric fields. Red and blue lines represent contours of spin-up and spin-down branches, respectively. Orange and green shaded regions represent spin-up and spin-down overpopulation for K and K’ valleys, respectively.

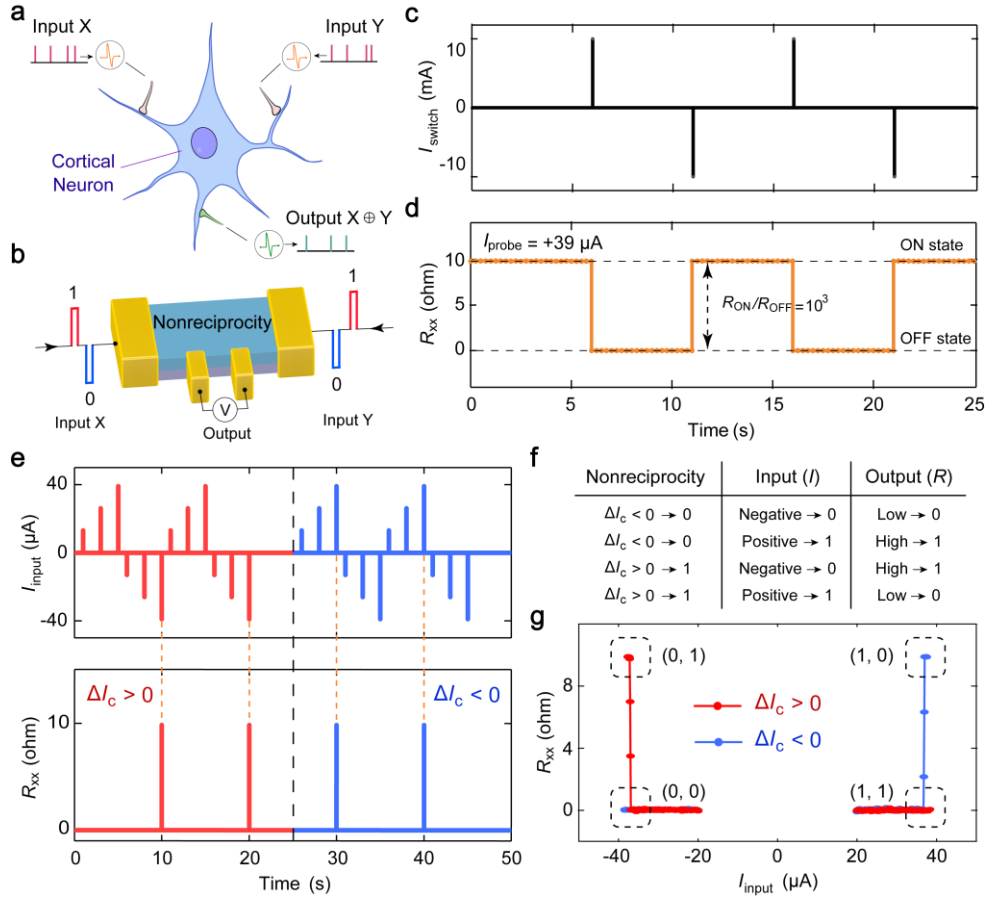


Fig. 4. Nonreciprocal neural transistor. **a**, Schematic structure of a biological cortical neuron. The neuron can classify linearly nonseparable inputs through the nonlinear XOR function. **b**, Schematic of the neural transistor. Input signals (represented by X and Y) are fed into the NbSe₂ film through the electrodes. **c**, Deterministic switching by a series of current pulses applied in the device. The width and magnitude of the current pulses are 200 μs and 10 mA, respectively. **d**, The resistance is measured by using a small d.c. excitation current of +39 μA . **e**, The responses of spike to the input current pulses for the polarity “+” and “-” states. **f**, Logic function of the neural transistor, in which nonlinear input-output responses depend on the polarity state. **g**, The XOR function in the nonreciprocal neural transistor. The dashed boxes represent the logic state values for input and polarity combinations (0,1), (1,1), (0,0) and (1,0), respectively.

Supplementary Information

Electrical switching of Ising-superconducting nonreciprocity for quantum neuronal transistor

Junlin Xiong^{1†}, Jiao Xie^{1†}, Bin Cheng^{2*}, Yudi Dai¹, Xinyu Cui¹, Lizheng Wang¹, Zenglin Liu¹, Ji Zhou¹, Naizhou Wang³, Xianghan Xu⁴, Xianhui Chen³, Sang-Wook Cheong⁴, Shi-Jun Liang^{1*}, Feng Miao^{1,5*}

¹Institute of Brain-Inspired Intelligence, National Laboratory of Solid State Microstructures, School of Physics, Collaborative Innovation Center of Advanced Microstructures, Nanjing University, Nanjing 210093, China

²Institute of Interdisciplinary Physical Sciences, School of Science, Nanjing University of Science and Technology, Nanjing 210094, China

³Hefei National Laboratory for Physical Science at Microscale and Department of Physics and Key Laboratory of Strongly Coupled Quantum Matter Physics, University of Science and Technology of China, Hefei, Anhui 230026, China

⁴Center for Quantum Materials Synthesis and Department of Physics and Astronomy, Rutgers, The State University of New Jersey, Piscataway, NJ, 08854, USA

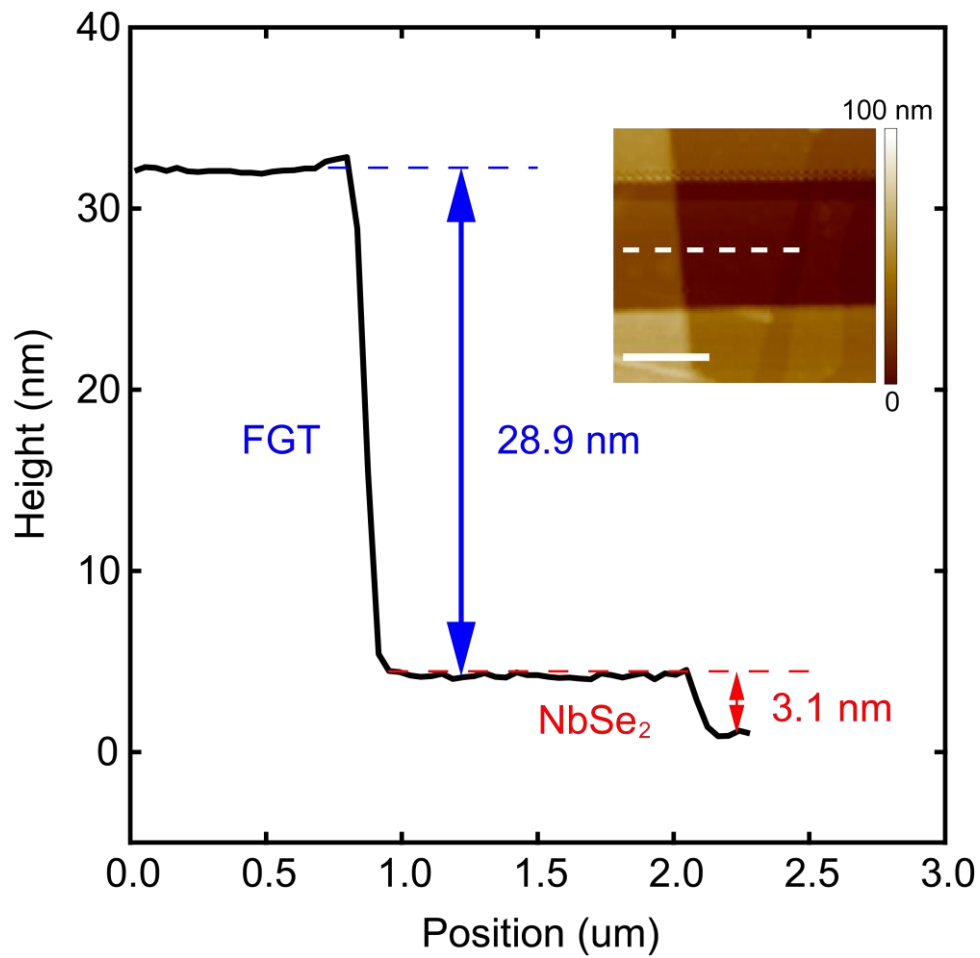
⁵Hefei National Laboratory, Hefei 230088, China

† Contribute equally to this work.

*Correspondence email: bincheng@njust.edu.cn; sjliang@nju.edu.cn; miao@nju.edu.cn

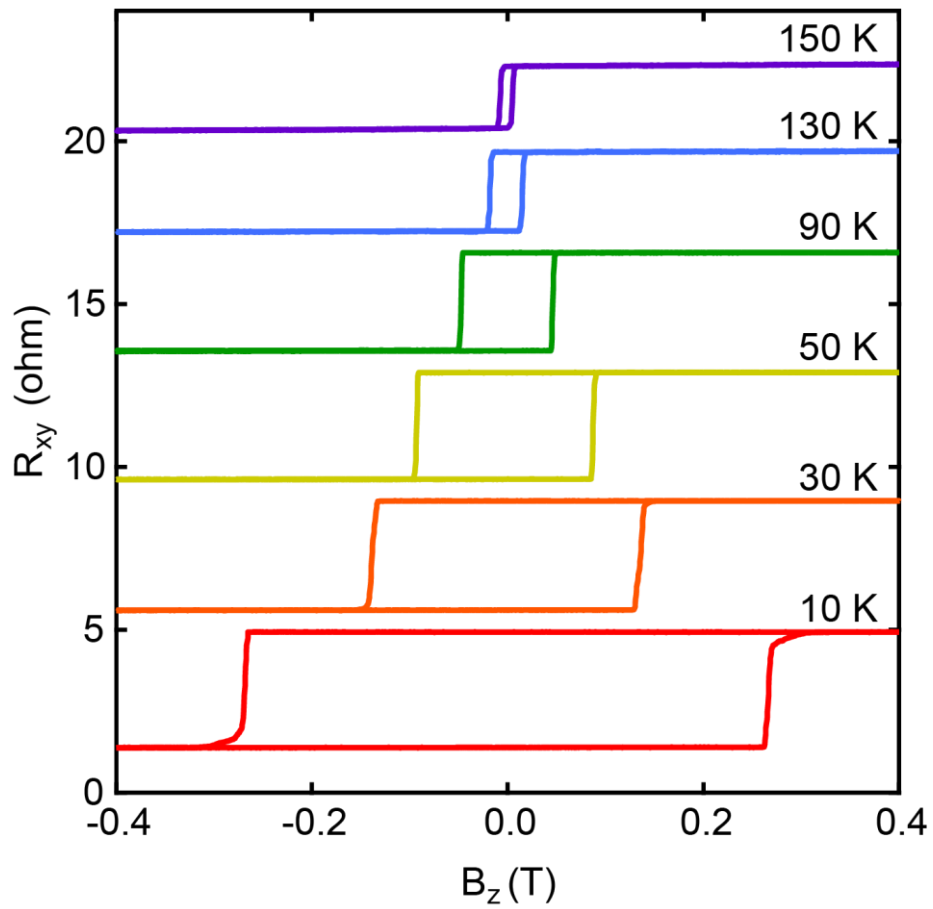
- I. Thickness of the PAIS device determined by atomic force microscope
- II. Anomalous hall effect for different temperatures
- III. Characterization of magnetic field dependence of superconductivity
- IV. Characterization of superconductivity with magnetic proximity
- V. Superconducting diode effect for different magnetization states under larger external magnetic fields
- VI. Second harmonic measurement for magnetization “UP” and “DOWN” state
- VII. Nonreciprocal superconducting transport at different temperatures
- VIII. Schematic of the mechanism for field-free electrical switching of perpendicular magnetization.
- IX. Reproducibility of the electrically switchable superconducting nonreciprocity and function of quantum neuronal transistor
- X. Comparison of magnetoresistance (MR) and resistance-area (RA) product between this work and previous literatures
- XI. Symmetry mechanism of electrically switchable superconducting nonreciprocity
- XII. Second harmonic generation measurements to determine crystallographic orientation

I. Thickness of the PAIS device determined by atomic force microscope



Supplementary Fig. 1. Height profile of the PAIS device determined by atomic force microscope. The FGT and NbSe₂ flakes are about 28.9 nm and 3.1 nm in thickness, respectively, as determined by atomic force microscope. AFM scanning position is represented by a white line in AFM image, shown in the inset. Scale bar is 1 μm.

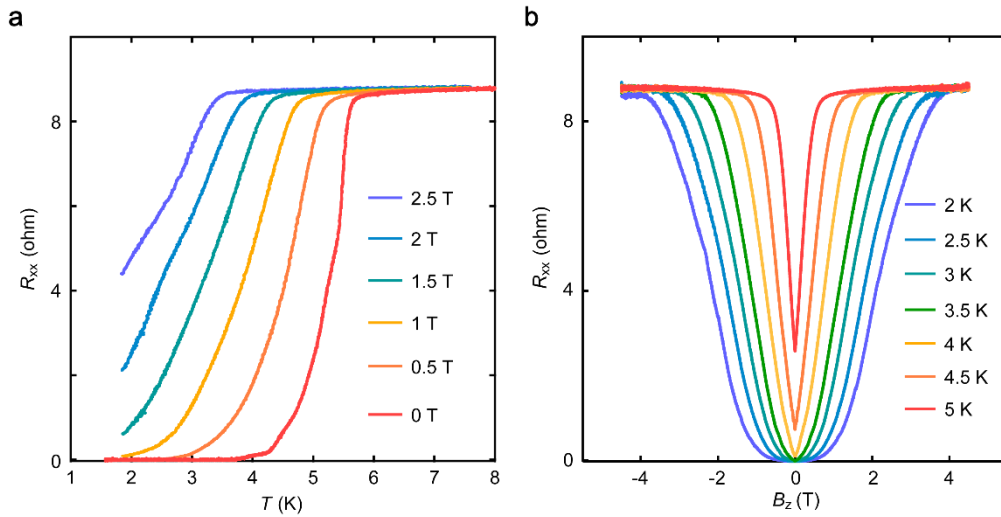
II. Anomalous hall effect for different temperatures



Supplementary Fig. 2. Hall resistance as a function of the perpendicular magnetic field for temperatures ranging from 10 to 150 K. The square-shaped hysteresis loop appearing at the low temperature indicates that the PAIS material possesses the perpendicular magnetic anisotropy.

III. Characterization of magnetic field dependence of superconductivity

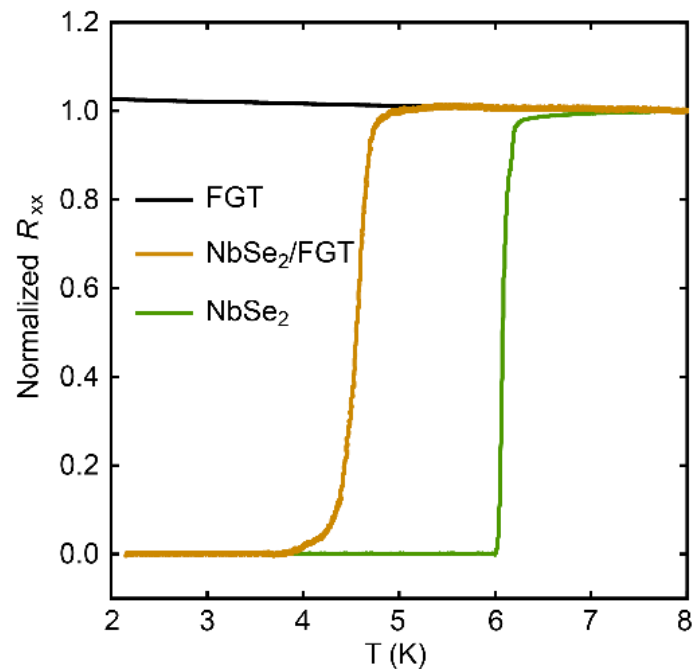
We characterized the transport properties of a PAIS device for different magnetic fields and temperatures (see Supplementary Fig.3a-b). As the applied perpendicular magnetic field or temperature increases, the superconductivity is suppressed.



Supplementary Fig. 3. Magnetic field and temperature dependence of the PAIS device resistance. **a**, Temperature dependence of the device resistance for magnetic fields ranging from 0 to 2.5 T. **b**, Magnetic field dependence of the device resistance for temperatures ranging from 2 to 5 K. This PAIS device consisting of seven-layer NbSe₂ flake was measured by applying an electrical current of 0.5 μ A.

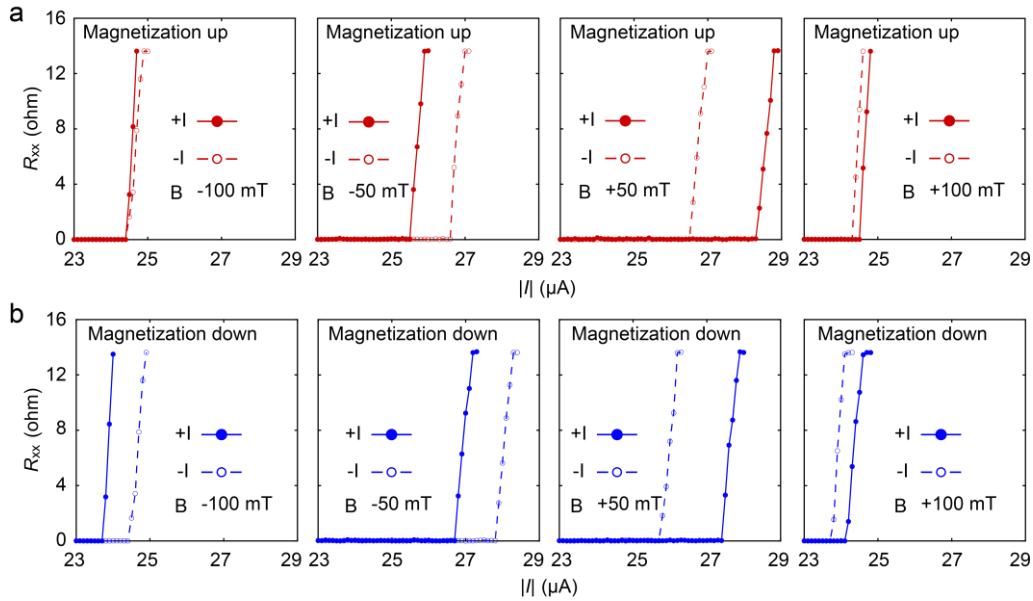
IV. Characterization of superconductivity with magnetic proximity

We measured the temperature dependent resistances of the NbSe₂, FGT and NbSe₂/FGT samples, with the corresponding results shown in Supplementary Fig. 4. The superconducting transition temperature T_c of the NbSe₂/FGT heterostructure with 7-layer (7L) NbSe₂ is 4.8 K and lower than that of the 7L-NbSe₂ sample (6.1 K), which can be attributed to the pair-breaking effect induced by the magnetization of FGT.



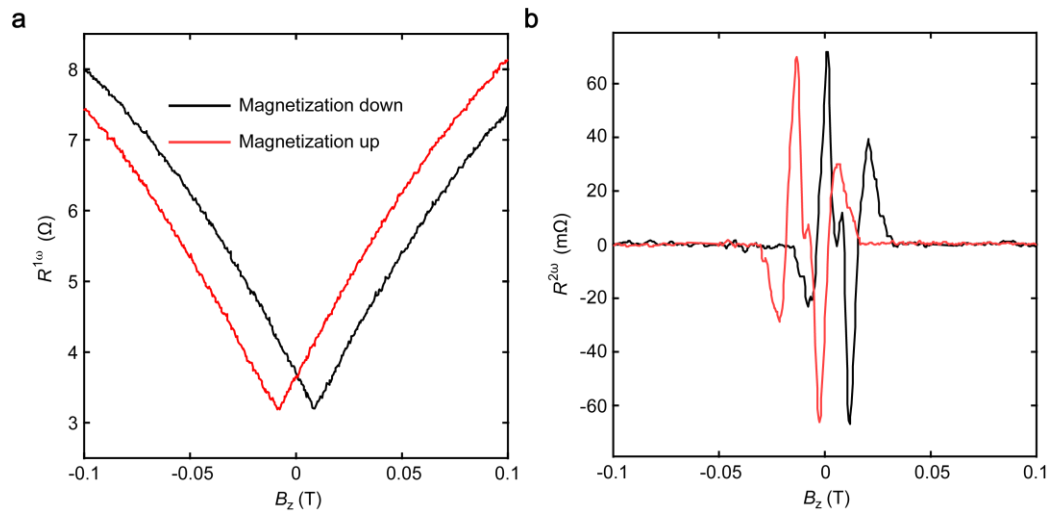
Supplementary Fig. 4. Temperature dependent normalized longitudinal resistances (defined as $R_{xx}(T)/R_{xx}(8K)$) of the NbSe₂ (green line), FGT (black line) and NbSe₂/FGT (orange line) samples.

V. Superconducting diode effect for different magnetization states under larger external magnetic fields



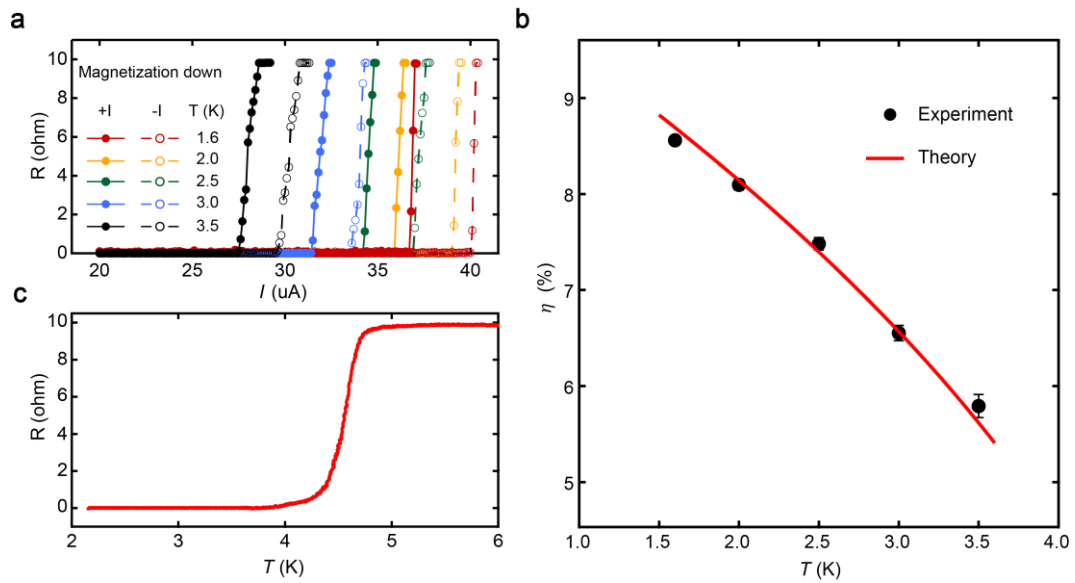
Supplementary Fig. 5. a, Current dependences of the resistance under different perpendicular magnetic fields $B = -100$ mT, -50 mT, 50 mT, and 100 mT for both positive and negative currents at 1.6 K when the magnetization is set as “UP” state. **b**, Current dependences of the resistance under different perpendicular magnetic fields $B = -100$ mT, -50 mT, 50 mT, and 100 mT for both positive and negative currents at 1.6 K when the magnetization is set as “DOWN” state.

VI. Second harmonic measurement for magnetization “UP” and “DOWN” state



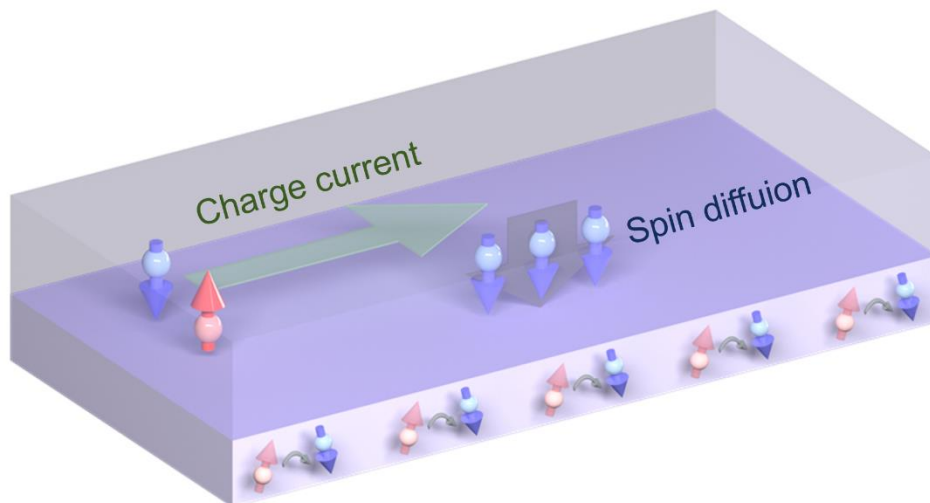
Supplementary Fig. 6. Second harmonic measurement for magnetization “UP” and “DOWN” state. **a**, The linear resistance R^ω as a function of the magnetic field for distinct magnetization states. **b**, The second-harmonic resistance $R^{2\omega}$ as a function of the magnetic field for distinct magnetization states. The red and black lines represent the cases for the magnetization “UP” and “DOWN” states, respectively.

VII. Nonreciprocal superconducting transport at different temperatures



Supplementary Fig. 7. Nonreciprocal superconducting transport at different temperatures when the magnetization is fixed as “DOWN” state. **a**, Current dependences of the resistance for both positive and negative currents at different temperatures ranging from 1.6 K to 3.5 K. **b**, The zero-field nonreciprocal efficiency η as a function of the temperature when the magnetization is fixed as “DOWN” state. **c**, The temperature dependence of the device resistance shows superconducting temperature $T_c \approx 4.8$ K.

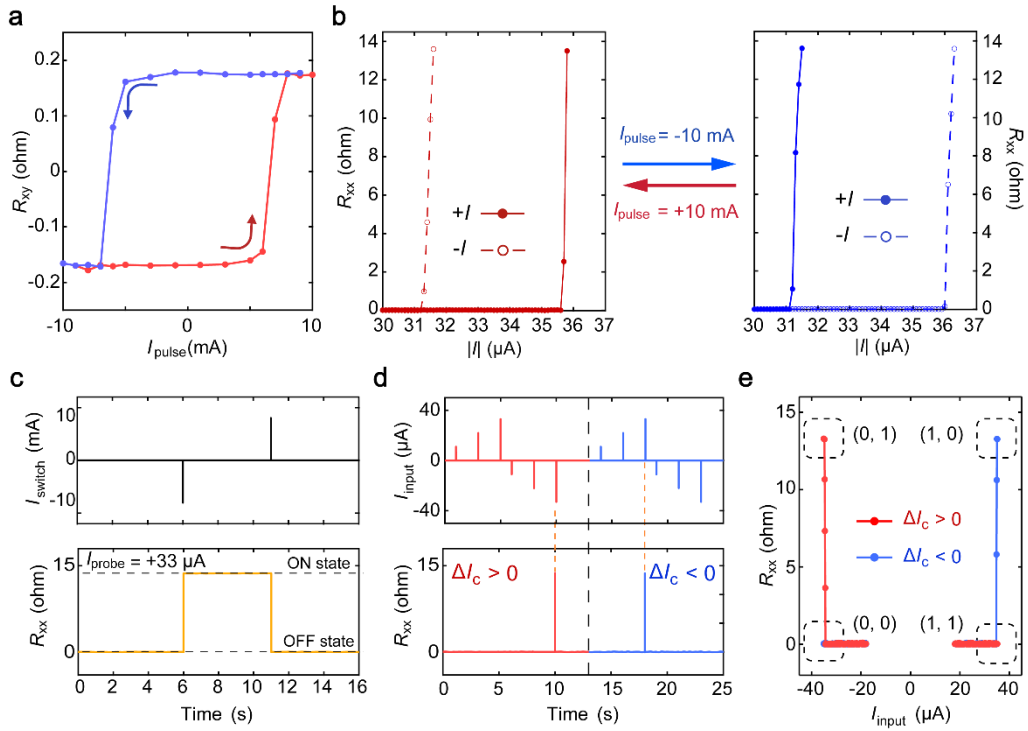
VIII. Schematic of the mechanism for field-free electrical switching of perpendicular magnetization.



Supplementary Fig. 8. Schematic of the mechanism for field-free electrical switching of perpendicular magnetization. The green arrow represents the electron flow (along the x direction), which generates out-of-plane spin polarization accumulating at the interface and diffusing into the magnetic layer. The current-induced spin polarization pointing in the z (-z) direction is indicated by the blue (red) arrows in the top layer. The red and blue arrows in the bottom layer represent the initial and resulting magnetization states.

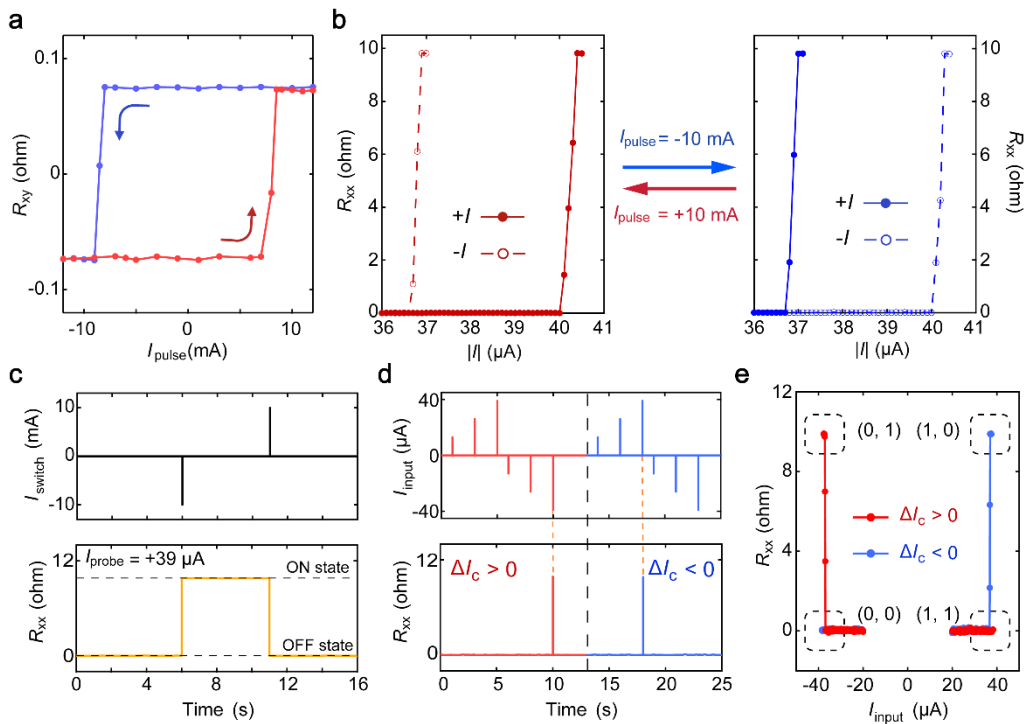
IX. Reproducibility of the electrically switchable superconducting nonreciprocity and function of quantum neuronal transistor

We fabricated three different devices with odd-layer and even-layer NbSe₂, respectively, and all the devices have the similar behaviors of electrically switchable superconducting nonreciprocity and function of quantum neuronal transistor, as shown in Supplementary Fig. 9-11.



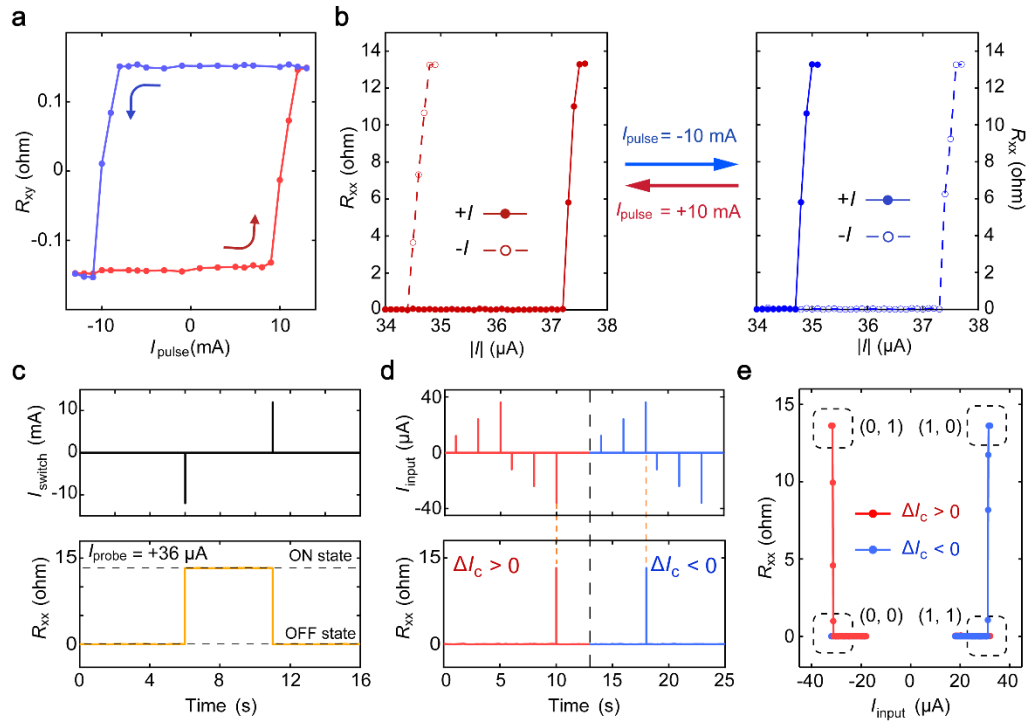
Supplementary Fig. 9. Electrically switchable superconducting nonreciprocity and functionality of nonreciprocal neural transistor in a five-layer device. **a**, Current-induced magnetization switching at zero field at 1.6 K. **b**, electrically switchable nonreciprocal superconducting transport. **c**, Deterministic switching by a series of current pulses applied in the device. The width and magnitude of the current pulses are 200 μ s and 8 mA, respectively. The resistance is measured by using a small d.c. excitation current of +33 μ A. **d**, The responses of spike to

the input current pulses for the polarity “+” and “-” states. **e**, The XOR function in the nonreciprocal neural transistor. The dashed boxes represent the logic state values for input and polarity combinations (0,1), (1,1), (0,0) and (1,0), respectively.



Supplementary Fig. 10. Electrically switchable superconducting nonreciprocity and functionality of nonreciprocal neural transistor in a seven-layer device. **a**, Current-induced magnetization switching at zero field at 1.6 K. **b**, electrically switchable nonreciprocal superconducting transport. **c**, Deterministic switching by a series of current pulses applied in the device. The width and magnitude of the current pulses are 200 μs and 10 mA, respectively. The resistance is measured by using a small d.c. excitation current of +39 μA . **d**, The responses of

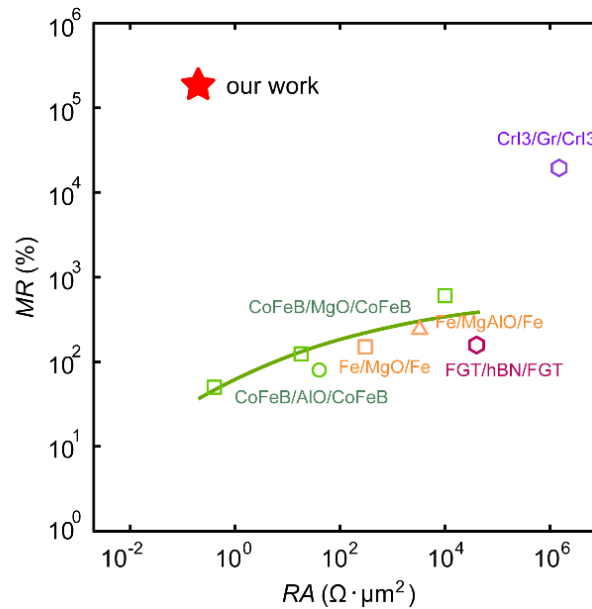
spike to the input current pulses for the polarity “+” and “-” states. **e**, The XOR function in the nonreciprocal neural transistor. The dashed boxes represent the logic state values for input and polarity combinations (0,1), (1,1), (0,0) and (1,0), respectively.



Supplementary Fig. 11. Electrically switchable superconducting nonreciprocity and functionality of nonreciprocal neural transistor in a six-layer device. **a**, Current-induced magnetization switching at zero field at 1.6 K. **b**, electrically switchable nonreciprocal superconducting transport. **c**, Deterministic switching by a series of current pulses applied in the device. The width and magnitude of the current pulses are 200 μs and 12 mA, respectively. The resistance is measured by using a small d.c. excitation current of +36 μA . **d**, The responses of

spike to the input current pulses for the polarity “+” and “-” states. **e**, The XOR function in the nonreciprocal neural transistor. The dashed boxes represent the logic state values for input and polarity combinations (0,1), (1,1), (0,0) and (1,0), respectively.

X. Comparison of magnetoresistance (MR) and resistance-area (RA) product between this work and previous literatures

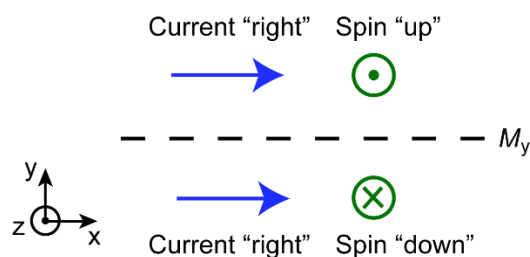


Supplementary Fig. 12. Comparison of magnetoresistance (MR) and resistance-area (RA) product between this work and previous literatures. Relationships between MR and RA of magnetic tunnel junctions (MTJs) with MgO-based (square)¹⁻³, AlO-based (circle)⁴, MgAlO-based (triangle)⁵ and van der Waals (vdW) material-based (hexagon)^{6,7} barrier are obtained from previous literatures. Different colors are used to distinguish different magnetic material components. The results from our work are denoted by the star symbol. The green solid line represents the tradeoff between MR and RA in the conventional MTJ. The RA of MTJ increases dramatically with the promotion of magnetoresistance.

XI. Symmetry mechanism of electrically switchable superconducting nonreciprocity

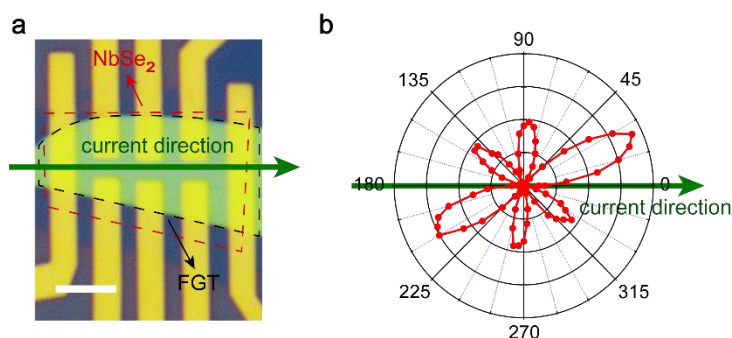
With the ubiquitous strain and lattice mismatch at the vdW interface and/or trigonal warping effect, lowering of C_3 symmetry breaks mirror symmetry M_y . On the one hand, the ubiquitous strain and lattice mismatch would break mirror symmetry M_y to generate the in-plane electric polarization P_y , but also break mirror symmetry M_x . In this way, the magneto-toroidal nonreciprocal directional dichroism (NDD) effect would be maximal due to an optimized nonreciprocal term $\hat{\mathbf{y}} \cdot (\mathbf{M}_z \times \mathbf{I}_x)$ and a maximum valley magnetization $\mathbf{P}_y \times \mathbf{I}_x$. On the other hand, with the current along the zigzag direction, the Hamiltonian with the trigonal warping effect, i.e., $H = \left(\frac{k_x^2 + k_y^2}{2m} - \mu \right) \sigma_0 + \lambda_I k_x (k_x^2 - 3k_y^2) \sigma_z$, would break the mirror symmetry M_y since $\mathcal{M}_y H \mathcal{M}_y^{-1} \neq H$. In contrast, the mirror symmetry M_x is preserved since $\mathcal{M}_x H \mathcal{M}_x^{-1} = H$. With the assist of the magnetization proximity, the M_y symmetry breaking allows to produce a finite momentum of Cooper pairs ($q_x = \frac{2\alpha_0}{3\alpha_3} |\mathbf{M}_z \times \hat{\mathbf{y}}|$), leading to superconducting nonreciprocity. Here, α_0 is $A_0(T - T_c)$ with the constant $A_0 > 0$, and α_3 is determined by Fermi surface properties of the Ising superconductor considering the trigonal warping effect. In addition, the current-induced z spin polarization that contributes to magnetization switching also requires this symmetry breaking, as shown in Supplementary Fig. 13. Therefore, as the current flows along the zigzag direction, these two effects (i.e., strain and lattice mismatch at the vdW interface, and trigonal warping effect) can coexist and simultaneously contribute to the

electrically switchable superconducting nonreciprocity.



Supplementary Fig. 13. Current-induced z spin polarization with the M_y symmetry preserved. The current in the x direction is unchanged while the spin in the z direction will be reversed under M_y symmetry operation.

XII. Second harmonic generation measurements to determine crystallographic orientation



Supplementary Fig. 14. Second harmonic generation measurements to determine the relationship between the current direction and crystallographic orientation. **a**, Optical image of a PAIS device. The scale bar is $3 \mu\text{m}$. **b**, Polar plot of the second harmonic generation (SHG) signal. The green arrow represents the current direction.

Supplementary References:

- 1 Parkin, S. S. P. *et al.* Giant tunnelling magnetoresistance at room temperature with MgO (100) tunnel barriers. *Nat. Mater.* **3**, 862-867 (2004).
- 2 Yuasa, S. *et al.* Giant room-temperature magnetoresistance in single-crystal Fe/MgO/Fe magnetic tunnel junctions. *Nat. Mater.* **3**, 868-871 (2004).
- 3 Ikeda, S. *et al.* Tunnel magnetoresistance of 604% at 300K by suppression of Ta diffusion in CoFeB / MgO / CoFeB pseudo-spin-valves annealed at high temperature. *Appl. Phys. Lett.* **93**, 082508 (2008).
- 4 Wei, H. X. *et al.* 80% tunneling magnetoresistance at room temperature for thin Al-O barrier magnetic tunnel junction with CoFeB as free and reference layers. *J. Appl. Phys.* **101**, 09B501 (2007).
- 5 Sukegawa, H. *et al.* Tunnel magnetoresistance with improved bias voltage dependence in lattice-matched Fe/spinel MgAl₂O₄/Fe(001) junctions. *Appl. Phys. Lett.* **96**, 212505 (2010).
- 6 Song, T. *et al.* Giant tunneling magnetoresistance in spin-filter van der Waals heterostructures. *Science* **360**, 1214-1218 (2018).
- 7 Wang, Z. *et al.* Tunneling Spin Valves Based on Fe₃GeTe₂/hBN/Fe₃GeTe₂ van der Waals Heterostructures. *Nano Lett.* **18**, 4303-4308 (2018).